https://doi.org/10.1016/j.cemconcomp.2022.104856

A multiscale study on gel composition of hybrid alkali-activated materials partially utilizing air pollution control residue as an activator

Muhammad Riaz Ahmad[1], Lan-Ping Qian[1], Yi Fang[1], Jian-Guo Dai[1]*

Department of Civil and Environmental Engineering, The Hong Kong Polytechnic University, Hung Hom, Kowloon, Hong Kong
Email: cejgdai@polyu.edu.hk (corresponding author)

A multiscale study on gel composition of hybrid alkali-activated materials partially utilizing air pollution control residue as an activator

Abstract

This paper provides a detailed underlying mechanism of gel composition of hybrid alkali-activated fly ash/slag (AAFS) pastes prepared by utilizing the air pollution control residue (APCr, a highly alkaline waste containing 38.3% of Na_2O content by mass) as a partial replacement (8%, 16% and 24% replacement by mass) of energy-intensive commercial sodium silicate (CSS) activator. AAFS pastes containing APCr as a partial replacement of CSS showed the strength, micromechanical and microstructure properties equivalent to the reference AAFS paste without APCr (R-0). SEM-EDS, FTIR spectral subtraction, and nanoindentation results showed that reaction products in AAFS pastes were composed of geopolymer gel (N-A-S-H), cross-linked gel (C-N-A-S-H) and alkali-activated gel (C-A-S-H) contributing to 60-66% of paste volume. Reaction products were more dominated by calcium-rich gels (C-A-S-H or C-(N)-A-S-H) as compared to N-A-S-H gel in all AAFS pastes. The heat of hydration and thermogravimetric results confirmed the slow rate of reaction of APCr-AAFS pastes at the early age but a higher rate of reaction at the silater stage which contributed to achieve a similar strength as control paste (R-0).

Key words

Air pollution control residue, alkali-activated materials, nanoindentation, selective dissolution, image analysis

1 Introduction

AAMs are regarded as a viable alternative cementitious binder to OPC owing to their sustainable nature during the production and superior engineering properties [1–3]. AAMs are produced by the reaction between an aluminosilicate source (precursors) and alkaline activators. Among the precursors, fly ash (FA) and blast furnace slag (GGBS) are intensively used due to their wide availability and fairly stable chemical composition [4–10]. The hybrid alkali-activated fly ash/slag (AAFS) binder provides the calcium source in the form of GGBS, which not only produces C-(A)-S-H gel but also contributes to the formation of (C)-(N)-A-S-H hybrid gel by partially replacing the sodium from the N-A-S-H gel, showing the higher extent

of cross-linking between the hydration products [11–14]. Among the activators, alkali hydroxides in combination with alkali silicates have been extensively studied as they produce the AAMs with the high compressive strength [5,7,15,16]. Alkaline activators particularly sodium silicate, which is produced by melting the silicon dioxide and sodium carbonate through an energy-intensive process at elevated temperatures (between 1200 and 1400°C), emits a large amount of CO_2, leading to negative environmental impact and mainly contributes to the high production cost of AAM [17]. Despite this, prior studies on AAMs have shown that carbon emissions from AAM-based concrete are 44-64% lower than that of OPC concrete for the comparable strength performance. According to the previous studies, alkali hydroxide and silicate in AAMs combined are responsible for nearly 60% of total greenhouse gases emission [2,18].

In the past few years, several studies have reported the preparation of waste-derived sodium silicate activators and hybrid activators [19–22]. AASA produced through the hydrothermal method requires elevated temperature between 150°C and 250°C for a higher rate of silica dissolution from glass cullets in the pressure reactor vessel [24]. AASA produced through the thermochemical method requires mixing NaOH and waste glass at very high temperatures ranging from 500° to 1300 C°. This method has a high rate of silica dissolution but still needs reheating of AASA at 175°C for an hour due to its partial solubility at ambient temperature [27–29]. Compared to the above processes, producing AASA from the reaction of sand/waste glass and NaOH is considered more feasible as it requires mixing and heating at 320°C for one hour [30]. Several other studies have also reported the preparation of AASA using NaOH with the combination of cleaning solution (CS) waste from the alumina industry [31], rice husk ash and silica fume [21], waste glass [28,30,32], sugar cane straw ash [33] and bottom ash [34]. This study, however, investigates the possible use of alkali-rich industrial waste "Air Pollution Control Residue (APCr)" as a partial replacement for commercial alkali silicate activator owing to its high content of Na_2O (38.3%).

APCr is a type of industrial waste generated during the treatment of dewatered sewage sludge (SS) from the waste-to-energy (W-t-E) plants and it is often transferred to landfills [35]. The treatment process of SS in the Hong Kong T-Park W-t-E plant and production of APCr is shown in Fig. 1 [36]. APCr consists of

fly ashes and solids collected downstream of gas treatment during the flue-gas cleaning process. It is composed of pollutants and soluble ions. It is highly corrosive, alkaline and classified as hazardous materials in several standards [37,38]. Hong Kong faces significant challenges not only with the recovery/recycling of resources but also with the disposal of wastes (e.g., incineration sludge ash, APCr) generated from these W-t-E plants. In this regard, incineration technology can significantly reduce the SS and municipal solid waste (MSW) volume by 85-90%. As APCr yield is estimated to be 2-6% of total waste burned [37], incineration of SS and MSW can produce APCr in a considerably higher amount and finding an alternative way to recover/recycle such kind of waste is very important.

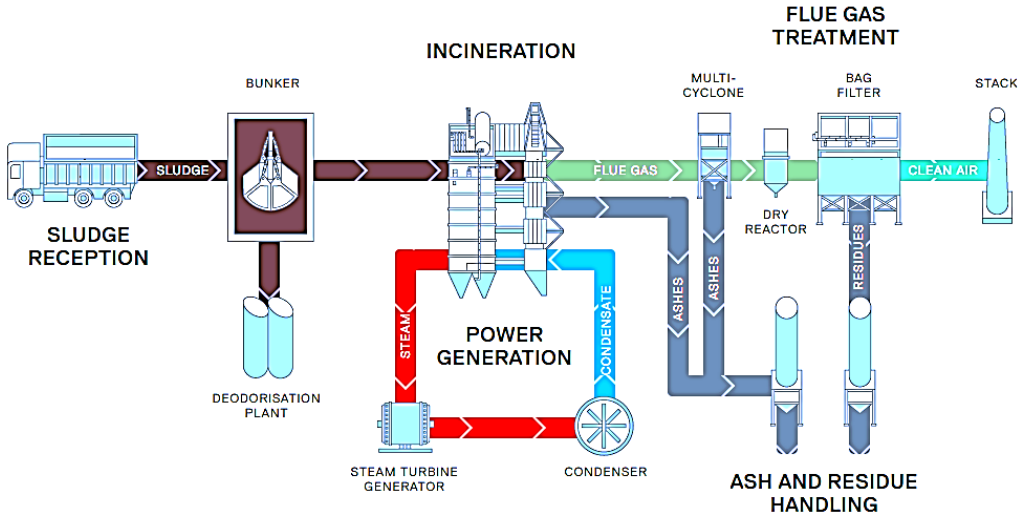

Fig.1. Sludge treatment process and production of APCr from W-t-E plant [36]

A few studies are available on the use of APCr in civil engineering [40–42]. Kourti et al. used glass-forming additives and DC plasma technology for the treatment of APCr to produce the precursors for AAMs [43,44]. A low-strength AAM (<10 MPa) was formed by mixing the APCr and co-fired fuel ash [45] through alkali-activation. After a careful review of available literature, authors have found that the use of APCr as an alkali-activator is not reported due to the absence of enough amount of alkali metals (Na or K) in its chemical composition. However, APCr produced in the Hong Kong W-t-E plant possesses a high content of alkaline oxides that are needed for the chemical activation of aluminosilicate precursors and slags. As

alkali-activators are a major source of carbon emission in AAMs and their production process is costly and energy-intensive, finding an alternative source of alkali-activators with minimal processing, low environmental impact and cost is an appealing alternative to the research community.

APCr being the source of alkali metals required for the activation of aluminosilicate precursor can be used as a potential alternative alkaline-activator (AAA). In this regard, this research aims to investigate the potential use of APCr as an AAA in the preparation of one-part AAMs. Before using the APCr to produce AAFS pastes, its heavy metal concentration and leaching characteristics were examined and it was classified as non-hazardous material. APCr was first dried in an oven at 105°C and then finely ground to powder in a ball mill machine. Later on, APCr was partially replaced with the commercial sodium silicate activator by 8%, 16%, and 24% by mass to prepare hybridly activated AAFS pastes. Besides introducing the APCr as an AAA to CSS, this study also provides significant insight into the gel composition of hybrid AAFS pastes through investigating the mechanical and microstructural (chemistry and mineralogy) properties by advanced material characterization techniques including calorimeter analysis, selective dissolution, image analysis, mercury intrusion porosimeter, nanoindentation, and SEM-EDS analysis.

2 Experimental Program

2.1 Raw materials

Alkali-activated fly ash/slag (AAFS) pastes were prepared by mixing the FA, GGBS, anhydrous commercial sodium silicate (CSS), and APCr. FA was obtained from the CLP power plant, Hong Kong while GGBS and sodium silicate were purchased from mainland China. APCr was obtained from the T-park incinerator facility in Hong Kong. APCr was dried in an oven at 105°C to remove any moisture content and then ground to a fine powder in a ball mill for 4 hours. Particle size distribution of FA, GGBS, and APCr was measured by the laser diffraction technique using Malvern Mastersizer 3000 and is presented in Fig. A1 (see Appendix). The average particle sizes of GGBS, FA and APCr were 14.1, 20.1 and 7.0 μm respectively. The chemical analysis of raw materials was performed by Rigaku Supermini200 through X-

ray fluorescence emission (XRF) technique and results are given in Table 1. The chemical composition of APCr indicates that it contains a high amount of alkali metals which can be helpful to chemical activate the aluminosilicate precursor. Moreover, the presence of Na_2O and SO_3 indicates the high amount of Na_2SO_4 in APCr, which has been reported as an alkaline activator in literature [46].

Table 1. Chemical analysis of GGBS, FA, APCr and CSS (%)

Oxides	Fly ash	GGBS	APCr	CSS
SiO_2	49.7	32.6	6.19	46.3
Al_2O_3	25.1	14.7	3.57	-
Fe_2O_3	9.58	0.35	4.65	-
CaO	7.84	42.4	3.27	-
MgO	2.8	6.53	1.71	-
Na_2O	-	-	38.3	50.7
K_2O	1.53	0.41	0.57	-
TiO_2	1.15	0.61	0.19	-
P_2O_5	0.84	0.18	3.02	-
SO_3	0.96	1.82	31.9	-
Others	0.5	0.4	6.64	3.0

XRD patterns of raw materials are provided in Fig. A2. A broad hump was found in XRD diagram of GGBS in the range of 25-35º 2θ which proves its high amorphous nature. FA mainly consists of mullite and quartz. Whereas, presence of thenardite (Na_2SO_4), trisodium phosphate (Na_3PO_4), and monosodium phosphate (NaH_2PO_4) was observed in APCr.

2.2 Preparation of AAFS pastes

Four AAFS pastes were prepared by mixing the GGBS, FA, CSS, and APCr. The ratio of FA and GGBS (0.8:0.2) was kept constant for all mixtures. The control mixture (named as R-0 paste or CSS-AAFS paste later in paper) was prepared by mixing the CSS with FA and GGBS. The CSS/precursor ratio for the R-0 was 0.12 (Na_2O/binder = 6.1%). For the other mixture, CSS was replaced 8%, 16%, and 24% with APCr (named as R-8, R-16, and R-24 pastes or APCr-AAFS pastes later in paper) by mass. APCr was introduced into the mixtures such that alkali content to binder ratio was same for all the mixtures (Na_2O/binder = 6.1%). Detailed mix proportions of AAFS pastes are shown in Table 2. CSS also contains some silica which is readily dissolved and contributes to improvement in the performance of AAFS at an early stage, however,

no extra silica source is introduced into mixtures containing APCr as AAA. Hence, the modulus ratio of activator was slight reduced due to the addition of APCr. To prepare the AAFS pastes, all raw materials were dry mixed in a Hobart mixer for 5 minutes. After that, water was added to the dry mixtures, and mixing was carried out at low speed for 2 minutes. Finally, the mixing was continued for another 3 minutes at high speed so that a uniform slurry was achieved. Fresh AAFS pastes were transferred to cubic molds of 40×40×40 mm^3 dimensions, vibrated on the vibration table for 1 min, and wrapped into plastic sheets to prevent moisture loss. Samples were taken out of molds after 24 hours, wrapped into plastic sheets, and then stored in the laboratory at room temperature.

Table 2. Formulations of AAFS paste expressed in terms of molar ratio

Mix Code	The overall molar ratio of Binder (B)				Activator			
	SiO_2/ Al_2O_3	CaO/ SiO_2i	Na_2O/ Al_2O_3	Na_2O/ SiO_2	Na_2O/B (CSS)	Na_2O/B (APCr)	Na_2O /B	SiO_2/ Na_2O
R-0	2.07	0.30	0.34	0.16	6.08	0	6.1	0.91
R-8	2.05	0.30	0.33	0.16	5.61	0.463	6.1	0.86
R-16	2.03	0.30	0.33	0.16	5.13	0.932	6.1	0.80
R-24	2.01	0.31	0.33	0.16	4.66	1.39	6.1	0.74

2.3 Testing methods

The influence of APCr as AAA on the mechanical and microstructure properties of AAFS paste was studied. Compressive strength of AAFS was determined at the 7, 14, 28, and 56 days using a compression testing machine, MATEST 3000 kN at a loading rate of 0.6 MPa/s. The compressive strength was calculated by taking the average of three samples.

When precursors and activator are brought into contact with water, an exothermic reaction occurs liberating a considerable amount of heat. The heat of hydration of AAFS pastes was measured by an Isothermal Calorimeter (Calmetrix I-Cal 4000) at a constant temperature of 20±0.1°C throughout the test. The weight of raw materials was 70 g for each AAFS paste and measured to a precision level of 0.001 g. AAFS paste slurry was prepared in a plastic container for 2 min outside the calorimeter and then placed inside the

chamber to record the heat flow and cumulative heat of hydration. The calorimeter test was performed for 14 days to study the rate of reaction at the early age (first 7 days) and later age after 7 days.

It is important to mention that age of tested specimens for all microstructural characterization techniques (SEM-EDS, nano-indentation, TGA, FTIR, MIP) was 28 days. Hydration reaction was stopped by immersing the samples in absolute ethanol for 7 days following the 28 days of ambient curing. After that samples were dried in a vacuum oven at 40°C for 24 h. A scanning electron microscope (SEM, Tescan Vega 3 XMU) equipped with EDS was used to study the hydration products. An epoxy resin was used to embed the AAFS paste samples under the vacuum condition. Samples were taken out of epoxy molds and were polished by Buehler (AutoMet 300) polisher. The surface of embedded samples was ground flat with the Grit 600 (5 mins) using water as a lubricant. After that, a smooth surface was obtained by polishing the samples with 9 µm, 5 µm, and 0.05 µm diamond/alumina grits (5 mins of polishing for each grit) using the MetaDi diamond suspension. Finally, samples were immersed in ethanol and put in an ultrasonic bath to remove any particles attached to samples. After polishing, samples were dried in a vacuum oven for 24 h, coated with a thin layer of carbon, and tested for SEM-EDS analysis. SEM analysis was performed at an accelerating voltage of 25 keV and a working distance of 15.0 mm in high vacuum conditions using back-scattered electron (BSE) imaging. The chemical composition of hydration products was quantitively studied by collecting 90 points for each AAFS paste through EDS point analysis. The point analysis was only performed in the gel regions and unreacted precursors were not included to study the gel composition. SEM-EDS mapping of AAFS pastes was also performed to investigate the distribution of different elements in the gel paste area.

Images analysis was performed on BSE images obtained from the SEM-EDS analysis using ImageJ software. The color threshold function of software was used to separate the different reacted and unreacted phases in AAFS pastes and a different color was assigned to each phase. Segmented images were then combined to produce the composite mapping of AAFS pastes and the percentage of each phase was

determined by the software based on the defined scale. It is to be noted that 4-5 different sites were chosen for the image analysis of each sample and then the average value was reported.

AAFS pastes were tested for nanoindentation which is regarded as an effective technique to measure the nano/micromechanical performance of hardened cement materials. Nanoindentation on AAFS pastes was performed by Bruker's TI 950 TriboIndenter. The samples for nanoindentation test were prepared according to a similar procedure as described for SEM-EDS analysis, however, polishing of samples was carried out for 30 min for each step to obtain a highly smooth surface. After polishing the sample, the surface roughness of each sample was determined by scanning probe microscopy (SPM) on the 50 µm × 50 µm area. The average RM roughness for R-0, R-8, R-16, and R-24 was 125.3 nm, 115.5 nm, 165.2 nm, and 153.7 nm respectively and SPM images are presented in Fig. 2. A square grid of 121 points (11 × 11) was chosen with a grid gap of 5 µm for indentation purposes. A trapezoidal loading and unloading program was selected. Loading was applied at a rate of 400 µN/s with a maximum load of 2000 µN/s. The maximum load was kept for 2 s and then unloading was completed in 5 s.

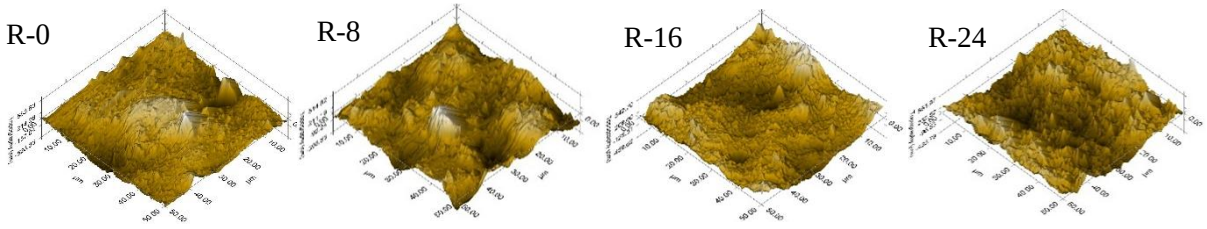

Fig. 2. Topography of polished samples measured through SPM imaging

Gel composition and reaction extent of precursors and activator was investigated through the selective dissolution process. Salicylic Acid/Methanol (SAM) extraction of AAFS paste was performed by dissolving 2 g of each AAFS paste powder (passed through a 75 µm sieve) and raw materials to SAM solution containing 120 ml of methanol and 8 g of salicylic acid. The mixture was stirred for 3 h using a magnetic stirrer and the suspension was vacuum filtered by Buchner funnel and a Whatman filter (0.2 um pore size). Insoluble residues were washed with methanol, dried in an oven, weighed, and then stored in a vacuum desiccator. SAM extraction of AAFS pastes only dissolves the C-(A)-S-H gel and any unreacted

precursor (GGBS and FA) and geopolymer gel (N-A-S-H) were not dissolved [14]. HCl extraction was performed to dissolve the geopolymer gel (N-A-S-H gel and zeolite). Unreacted FA and silica gel were left as insoluble residues during this process [14]. However, HCl extraction also decomposes C-S-H by removing the Ca^{+2} and leaving the silica gel behind. Slag is completely dissolved in this process. HCl extraction was performed by adding 1 g of AAFS paste into 250 ml of HCl (1:20). The reactivity of alkaline activator was studied by dissolving the AAFS pastes (2 g) into distilled water (200 g) for 3 hours at 25°C in an ultrasonic bath. After the dissolution, solutions were centrifuged at 10000 rpm for 10 minutes to separate the residues from the liquid. Fourier-transform infrared (FTIR) analysis was performed on original AAFS pastes powders, water residues, HCl residues and SAM residues by using the instrument PerkinElmer UATR-two. The analysis was performed in an absorption mode at 2 cm^{-1} resolutions. Spectral subtraction technique was used to study the dissolution of reaction products in AAFS pastes. The HCl and SAM residues spectra were subtracted by the original AAFS powder spectra to obtain the spectra for the dissolved reaction products due to HCl and SAM selective dissolutions. Spectral subtraction was performed using the OMNIC software.

Thermogravimetric analysis (TGA) on AAFS paste powder samples was conducted by Rigaku Thermo Plus EVO2 equipment. The mass for each paste powder sample was around 10 mg. The temperature was increased from 30°C to 1000°C for all powder samples at a heating interval of 10°C/min. Mercury intrusion porosimeter (MIP, AutoPore IV 9500) was used to study the pore structure of AAFS pastes. AAFS pastes were broken into particle sizes of 2.36-5.0 mm and were dried using a freeze dryer for 48 hours at a temperature of -85°C and vacuum pressure of 0.133 mBar. After that samples were placed in a vacuum oven at 20°C until tested for MIP analysis.

3 Results and Discussion

3.1 Compressive Strength

The development of compressive strength of AAFS pastes with the age is shown in Fig. 3. At the early age of 7 days, the compressive strength of control AAFS paste (R-0) was 50.5 MPa and higher than the other APCr-AAFS pastes in which CSS was replaced by 8%, 16%, and 24% APCr. However, the strength of R-8, R-16, and R-24 pastes at 28 days was 63.2, 61.5, and 63.5 MPa and comparable to the strength of control paste (R-0) of 62.2 MPa. At 56 days, the strength of R-0, R-8, R-16, and R-24 was 68.5, 69.2. 68.5 and 73.6 MPa and therefore, the rate of increase in strength from 7 days to 56 days was 35.6%, 41.3%, 66.5%, and 73.2% respectively. Although, the dissolution of APCr in AAFS pastes at an early age was slower as compared to CSS, its contribution to the development of strength was more obvious at 28 days and 56 days. APCr could successfully replace the CSS partially while producing the AAFS pastes with a similar or slightly higher strength up to a replacement level of 24% given that alkali content (Na_2O/binder) in paste is kept the same. As compared to APCr based AAA, alkali metal and silica in the CSS (SiO_2/ Na_2O = 0.91) could quickly dissolve into the water due to its amorphous nature and react with the precursors to form the hydration products which can increase the strength of control AAM paste (R-0) at an early age. AAFS pastes containing APCr closed the strength gap with the control AAFS paste (R-0) with the increase in curing age as a result of continuous reaction at a later stage. It was also observed that the APCr-AAFS pastes showed comparable performance to the pastes prepared with CSS. Hence, the influence of silica modulus (SiO_2/ Na_2O, between 0.91-0.74) was more pronounced on the early age properties of pastes but diminished at a later age. However, previous studies have shown that a more significant change in silica modulus (e.g. 0.5, 1.0, 1.5, 2.0) can significantly influence the mechanical properties [15,16,47]. Alnahhal et al. [21] used the NaOH and rice husk ash to prepare AASA and compared its strength with AAFS pastes prepared with CSS while keeping the Na_2O/binder the same. The results concluded that rice husk ash based AASA could provide comparable strength to the CSS activator given the content of alkalis and silicates of activators were kept in similar proportions.

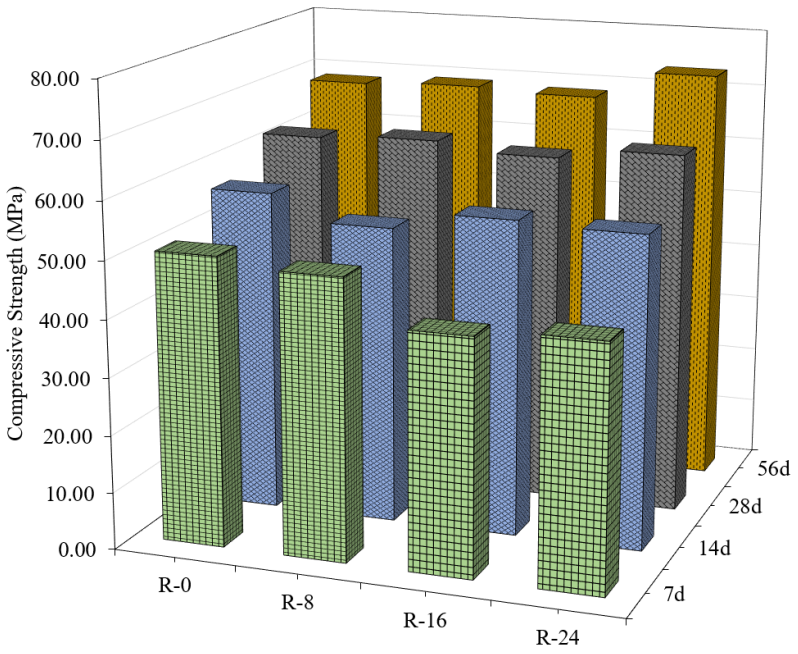

Fig. 3. Development of compressive strength of AAFS pastes

3.2 Reaction kinetics of AAFS pastes

Reaction kinetics of AAFS pastes were studied by the calorimetric analysis. Results of heat evolution and cumulative heat flow starting from the mixing time (2 min) to 14 days are shown in Fig. 4. An initial peak with the massive heat flow in all AAFS pastes was observed during the first few hours (Fig. 4a). The second major and acceleration peak started appearing around 14 h and reached the peak at 24 h after mixing although with significantly low intensity as compared to the initial peak (Fig. 4b). The third peak appears after 36.7 hours of mixing but this peak was dominated by the AAFS pastes containing R-24 (as shown in magnified images at Top middle of Fig. 4b). The first peak is primarily associated with the wetting and dissolution of precursors (mainly T-O and Me-O bonds of slag particles at the early stage) in the first few minutes and partly with the formation of early reaction products due to dissolved units of Ca, Na, and Si in solution. The heat evolution was highest for the control AAFS paste (R-0) showing a higher amount of dissolution of precursors at the early stage [4,48]. The second peak shows that a higher amount of hydration heat was released for R-0 paste during the first 24 hours (hence, the first and second peaks are dominated by R-0 paste). Sodium silicate which is a highly amorphous material quickly dissolves (releasing Na and Si) into the water and helps to form the reaction products at an early age. The emergence of second and

third peaks was associated with the formation of hydration products C-A-S-H and C-(N)-A-S-H during the condensation process. The start of second peak also corresponds to the setting time of AAFS pastes. After these major peaks, the heat of hydration decreases to a large extent for all pastes due to a slow reaction rate at a later stage. The heat flow rate was higher for the R-24 paste, followed by R-8, R-16 and R-0 respectively, suggesting that more reaction products were formed in the APCr based AAFS pastes at a later stage as compared to control paste R-0 (as shown in magnified images at bottom right corner of Fig. 4b). These findings are also in line with the compressive strength results of AAFS pastes, i.e., gain in compressive strength was slower at an early age for APCr activator based pastes however they achieved a similar compressive strength to control paste with the increase in time which is attributed to higher rate of reaction of APCr at a later stage.

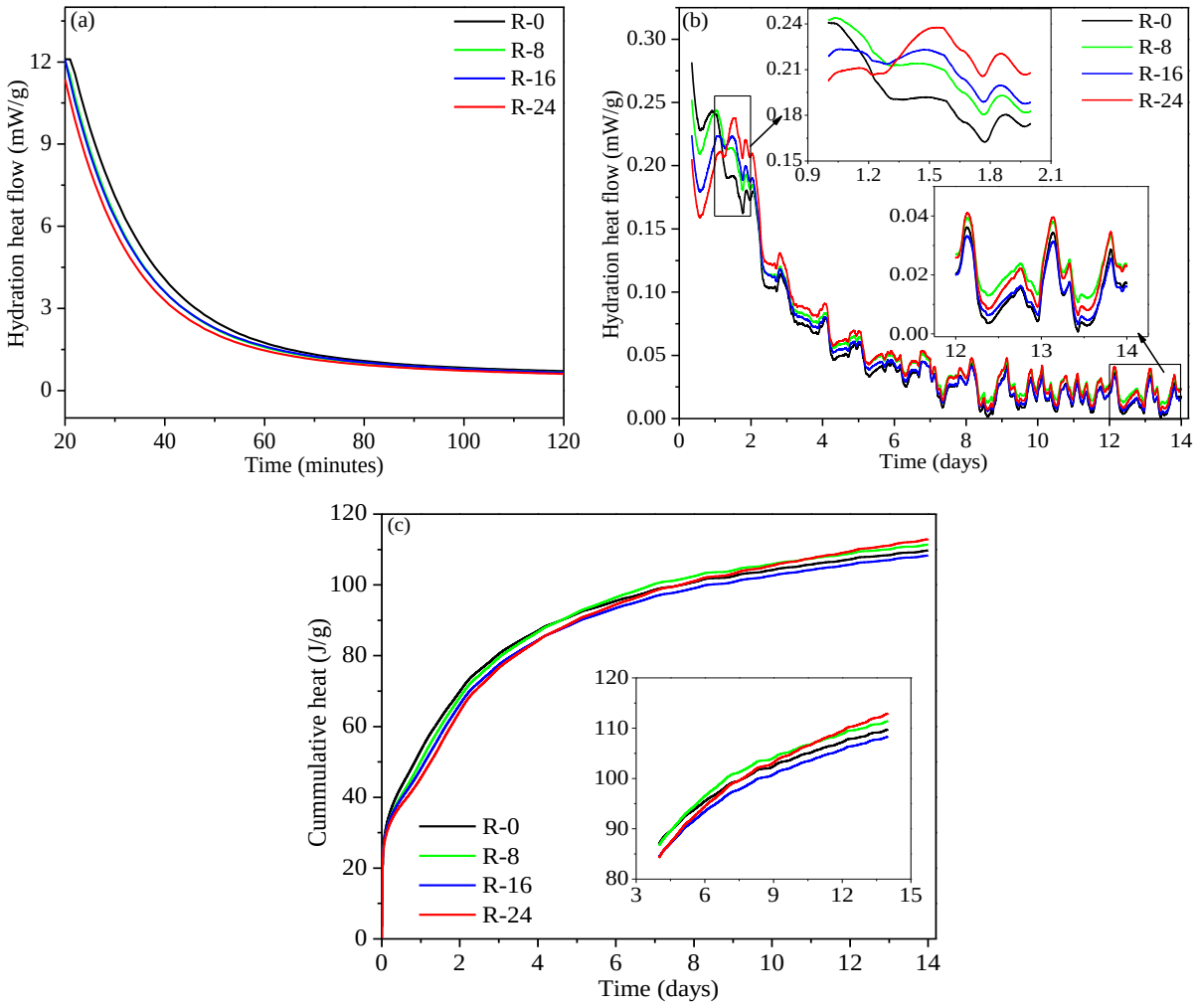

Fig. 4. Calorimetric analysis of AAFS pastes (a) Hydration heat flow during the first 120 mins, (b) hydration heat flow from 2 h to 14 days, and (c) Cumulative heat flow

The influence of APCr as a partial replacement of CSS on the cumulative heat of AAFS paste is shown in Fig. 4c. The sharp increase during the early stage is due to wetting and dissolution of precursors (mainly slag) in an alkaline environment. Control paste (R-0) showed the highest cumulative heat curve starting from the mixing to the first few days. At a high silicate modulus of 0.91, more dissolved Si is available from the CSS and also a higher amount of Ca, Si and Al from slag which can form higher amount of reaction products at an early stage. When CSS is replaced by APCr, silicate modulus is slightly decreased to 0.74, which in turn increases the alkalinity of the mixture. The higher alkalinity can increase the reaction rate of both fly ash and slag thus increasing the dissolution of alumina and silica in mixtures having lower silicate modulus at a later age. Gao et al. [49] have reported that for the fixed FA/GGBS, a decrease in silicate modulus resulted in higher total heat. However, change in cumulative heat among the different AAFS pastes was not significant in this study as silicate modulus among the different pastes did not vary to a large extent. Cumulative heat after 14 days of heat of hydration test was 109.75, 111.4, 108.32, and 112.94 for the R-0, R-8, R-16, and R-24 respectively, it shows that APCr based AAFS pastes produced equivalent or slightly higher amount of reaction products as compared to control paste. It is also worth mentioning that the results of calorimeter test corroborated the strength results of AAFS pastes.

3.3 Pore structure of AAFS pastes

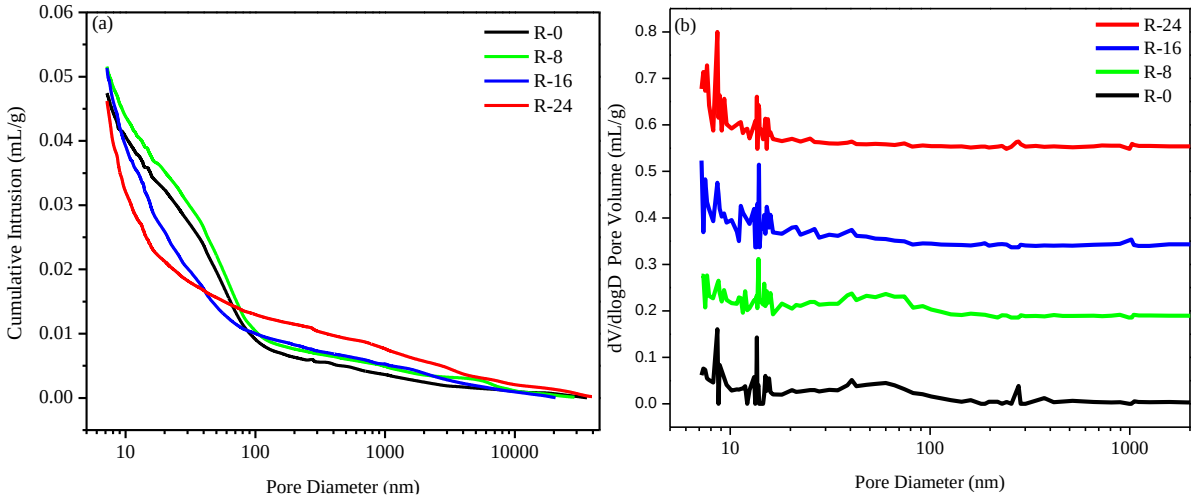

Fig. 5. MIP analysis of AAFS pastes (a) Cumulative pore volume distribution and (b) differential pore size distribution

The pore structure of AAFS pastes determined by MIP analysis is given in Fig. 5. The relationship between the cumulative intrusion volume and pore diameter is plotted in Fig. 5a. Cumulative intrusion values of R-0, R-8, R-16 and R-24 were 0.0474, 0.0516, 0.0514 and 0.0462 mL/g, which corresponds to porosity value of 8.88%, 9.44%, 9.26% and 8.31% respectively (Table 3). The porosity and average pore diameter of R-24 paste were the lowest among all pastes which confirms that R-24 paste showed slightly denser microstructure as compared to other AAFS pastes. The pore structure (Fig. 5b) of pastes showed that the size of most of the pores is below 100 nm. Pore size distribution of pastes determined by MIP analysis is plotted in Fig. 6. In cement-based materials, pores are generally classified into four types, gel pores (pore size < 10 nm), transitional pores (pore size, 10-100 nm), capillary pores (100-1000 nm), and macropores (>1000 nm). Capillary pores can influence the strength and permeability of the matrix whereas transitional and gel pores influence the durability, strength, and shrinkage [50]. The pore size distribution is studied by dividing them into small size pores (<100 nm) and large size pores (>100 nm). The small size pores can be related to the reaction products of paste. The volume of small size pores in the R-0, R-8, and R-16 were about 81.1, 80.2, and 80.6% respectively. The volume of gel pores slightly increased from 14.9% (in R-0) to 15.6% (in R-8) and 24.3% (R-16). For the R-24 paste, the volume of small pores was decreased to 72% but, a further increase in gel pores (31.4%) was observed. Although R-24 contains a higher volume of larger size pores (> 100 nm), its strength at 28 days was similar to other pastes. The negative effect of higher volume of large size pores was balanced by the higher volume of gel pores. The higher volume of gel pores points that the higher amount of gel phases (C-A-S-H, N-A-S-H or C-N-A-S-G gels) were formed in the paste containing APCr and contributed to strength [5].

Table 3. Pore structure characteristics of AAFS pastes determined by MIP

Sample	R-0	R-8	R-16	R-24
Total Intrusion Volume (mL/g)	0.0474	0.0516	0.0514	0.0462
Porosity (%)	8.88	9.44	9.26	8.31
Average Pore Diameter (nm)	23.4	23.6	17.5	16.5

Bulk Density (kg/m^3)	1867	1830	1797	1798
Skeletal Density (kg/m^3)	2055	2021	1986	1961

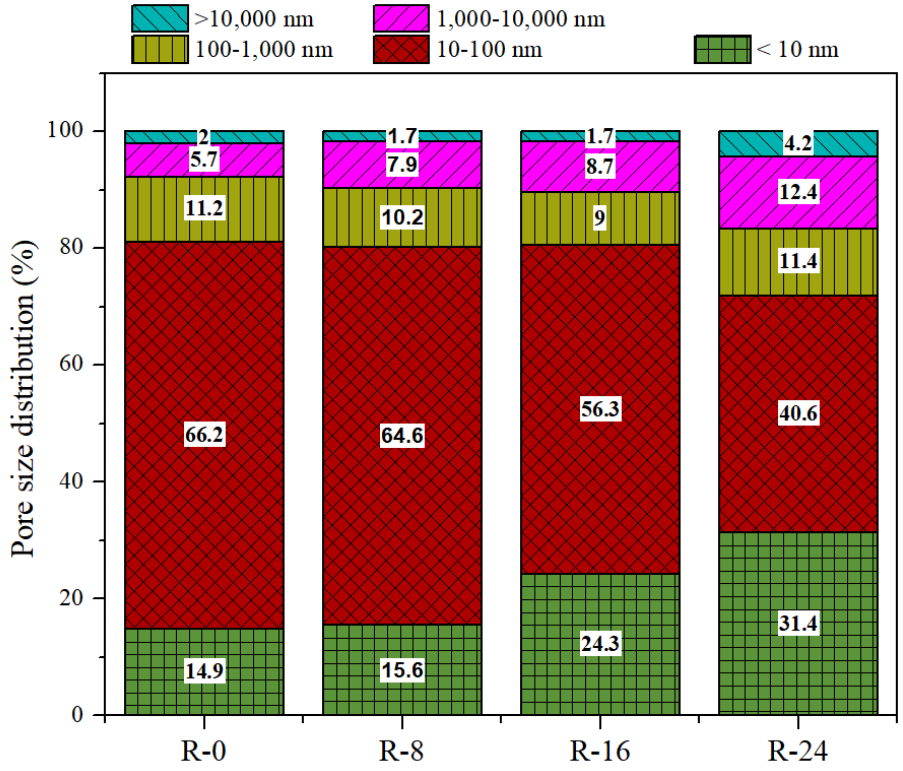

Fig. 6. Pore size distribution of AAFS pastes

3.4 SEM-EDS Analysis

3.4.1 Gel chemical composition by SEM-EDS analysis

Reacted and unreacted phases were studied by SEM-EDS technique in detail. First of all, reaction products were identified by different grey scale levels and then their chemical compositions were studied by the EDS point analysis and ternary diagram. The grouping of different atomic ratios of AAFS pastes was further studied by the statistical analysis. Finally, the SEM-EDS mapping of AAFS pastes was conducted to examine the dispersion of major elements and homogeneity of reaction products.

Different phases (reaction products and unreacted phases) are identified by back scattered electron (BSE) imaging as shown in Fig. 7. Area 1 shows the reaction products (gel phases) and predominantly consisted of N-A-S-H/C-A-S-H gels in all pastes. Unreacted FA, GGBS, and Fe particles are highlighted by areas 2,

3, and 4 respectively. The reaction of FA particles (complete and partial dissolution of FA) is highlighted by area 5.

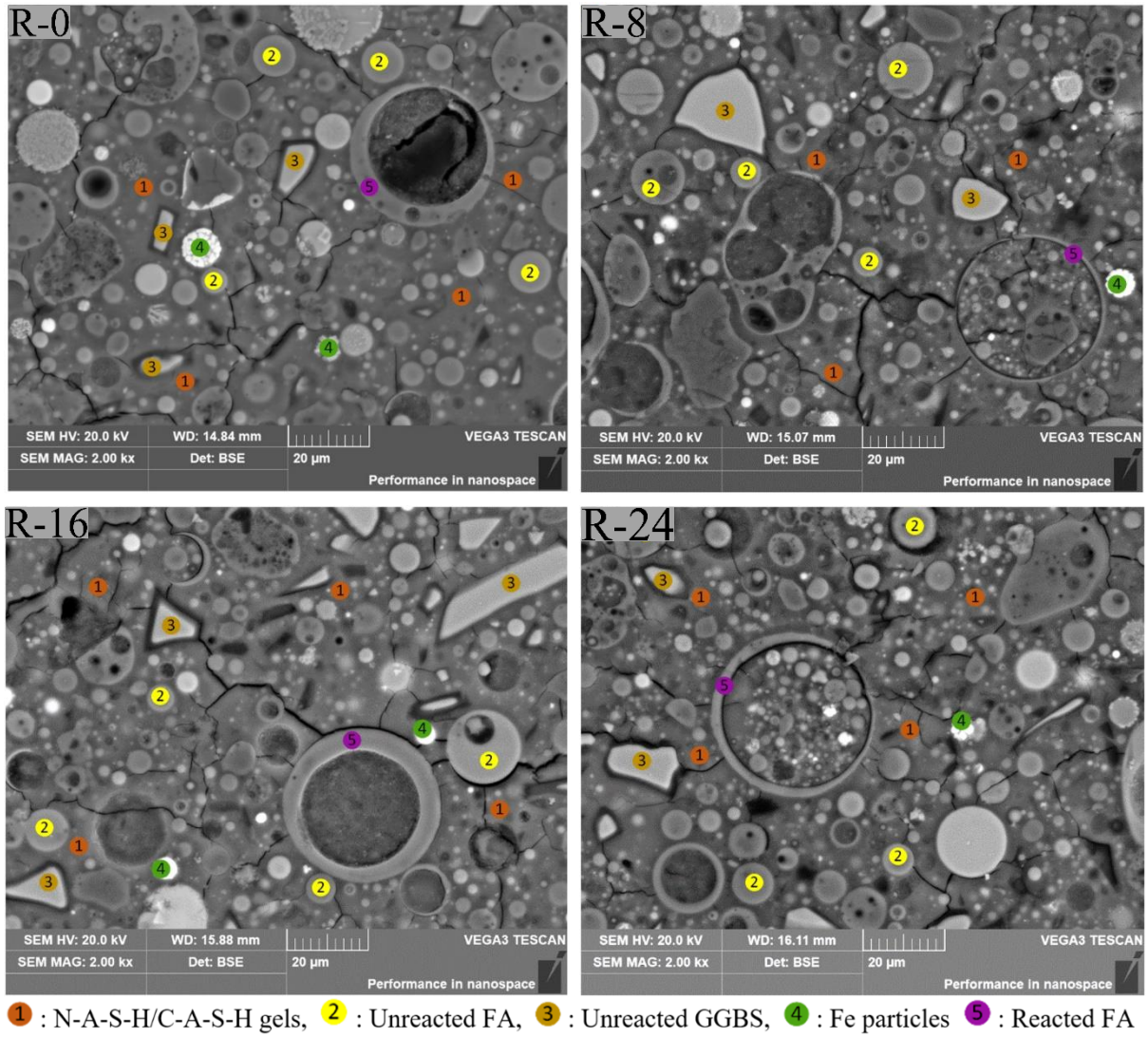

Fig. 7. BSE images of AAFS pastes

The chemical composition of gels pastes (reaction products), raw precursors (raw FA and GGBS) and unreacted FA and GGBS in paste samples via SEM-EDS analysis is given in Table 4. For the raw FA, the starting Si/Al ratio was 1.75, which was slightly reduced to 1.67 for the unreacted FA particles in the pastes, whereas the Ca/Si ratio (0.24-0.25) both in raw and unreacted FA was nearly the same. Hence, the unreacted FA particles in paste did not dissolve or show leaching of any major element to form reaction products and it shows that some of the FA particles are inert by nature which can have physical effect by filling the

micropores. For the apparently unreacted GGBS particles, the Ca/Si ratio decreased from 1.99 to 1.21 as compared to raw GGBS. This shows that some of the Ca from the GGBS had reacted or leached in the paste system to form the reaction products, however morphology of particles did not change significantly. The Si/Al ratio was slightly increased from 1.96 to 2.09 showing the interaction of Al phases from FA with the GGBS particles in the presence of an activator.

The results of each AAFS paste are reported by taking the average of at least 90 points on the gel pastes. For the control paste (R-0), the average Ca/Si ratio of gels was 0.37, which was slightly higher as compared to R-8 (Ca/Si = 0.33) while lower as compared to R-16 (0.44) and R-24 (0.39). However, the Si/Al ratio in the control paste (R-0, Si/Al = 2.52) was higher as compared to R-8, R-16, and R-24 (Si/Al ≈ 1.95-2.28). The Na/Si (0.27) and Na/Al (0.65) ratios in the control paste were also higher than the pastes containing APCr (Na/Si ≈ 0.24-0.27 and Na/Al ≈ 0.50-0.58). These findings indicate that the chemical composition of gels or reaction products for the different pastes did not vary significantly and were of similar nature. Either both types of gels (C-A-S-H and N-A-S-H) were present in all AAFS pastes or they were highly cross-linked (C-N-S-A-H) with each other. However, quantification of different gels is not possible due to the same grey scale level for all types of gels. The formation of N-A-S-H gel along with the C-A-S-H gel for geopolymer containing 20% GGBS content has also been reported in the literature [48]. As SEM-EDS was conducted on point level, it is suggested cross-linked gel was formed in significant amount due to the presence of all major elements participating in the gel composition (Na, Ca, Si, and Al). Due to the higher Ca/Si ratio in R-16 and R-24, both of these pastes show the presence of a slightly higher amount of Ca-rich C-A-S-H gel as compared to R-0 and R-8.

Table 4. The average elemental ratio of AAFS pastes determined from the SEM-EDS analysis

Sample name	Ca/Si	Si/Al	Na/Si	Na/Al
Raw FA	0.24	1.75	-	-
Unreacted FA in pastes	0.25	1.67	0.08	-
Raw GGBS	1.99	1.96	-	-
Unreacted GGBS in pastes	1.21	2.09	0.03	-
R-0	0.37	2.52	0.27	0.65

R-8	0.33	1.95	0.27	0.55
R-16	0.44	2.28	0.26	0.58
R-24	0.39	2.21	0.24	0.50

A ternary diagram of the ratio of Na, Al Ca normalized by the Si quantity is plotted in Fig. 8 for the unreacted fly ash and GGBS particles and gel in the paste. The ternary diagram has been used in many studies to quickly identify the gel composition of alkali-activated materials. The presence of different kinds of alkali-activated gel (C-A-S-H), low and high calcium geopolymer gels (N-(C)-A-S-H), and cross-linked gels (C-N-A-S-H) has been highlighted in the diagram [13,48,51,52]. In total, 348 points (almost 90 from each paste) from the gel were selected to plot the ternary diagram. Unreacted GGBS and FA particles are also included in the diagram. It can be noticed that some GGBS particles have similar composition reaching to that of the gel indicating that they had undergone partial reaction to form the C-A-S-H gel. Two main types of gels can be identified in all AAFS pastes: (a) High calcium gel/ alkali-activated gel (C-A-S-H) and (b) Co-existence of both C-A-S-H and N-A-S-H gels dominated by both Na and Ca phases (Cross-linked gel, C-N-A-S-H).

The EDS data was further used to statistically analyze the influence of elemental ratio on the composition of gels by Tukey test [53]. A comparison of the atomic ratios of gel composition was made to determine if there were significant differences among the atomic ratio of different gels with a confidence interval of 95% [54]. Summary of the statistical analysis is presented in Table 5. The ratio of Ca/Si clustered between the 0.07 to 0.44 for the control paste (R-0), which was between 0.14 to 0.49 and 0.04 to 0.48 for R-16 and R-24 respectively (max values were ignored as they were quite far from 3rd quartile). However, the ratios of Si/Al and Na/Al from the minimum ratio to the 3rd quartile for the R-0 were slightly higher as compared to the pastes containing APCr. The Na/Si atomic ratio from the minimum to 3rd quartile for all the pastes showed very minor variation. Based on the atomic ratio of gel elements, the grouping of different atomic ratios is shown in Table 5. Results show that both R-0 and R-24 belong to the same groups in terms of the Ca/Si (group B) and Si/Al (group A) ratios, suggesting the presence of similar nature of cross-linked gel was dominated by Ca-rich phases (C-(N)-A-S-H). The molar ratio of Na/Si and Na/Al was higher in R-0,

R-8 and R-16 AAFS pastes as compared to R-24 paste and all of them fell in group B. However, the presence of geopolymer gel (N-A-S-H) in all pastes was dominated by calcium-rich phases. This confirms that cross-linked gel (C-N-A-S-H) was infact present in the all AAFS pastes as also shown by nanoindentation results. A visible difference between the atomic ratios can be seen with the wide dispersion (higher difference between the min and max values) and overlapping. However, the 1st and 3rd quartiles along with the median can be used to examine if the data have wide dispersion. In principle, no big difference was observed in the gel composition of AAFS pastes due to the replacement of CSS by APCr by 8%, 16%, and 24%. This shows the efficacy of APCr to partially replace the CSS in the preparation of AAMs to achieve the same mechanical performance.

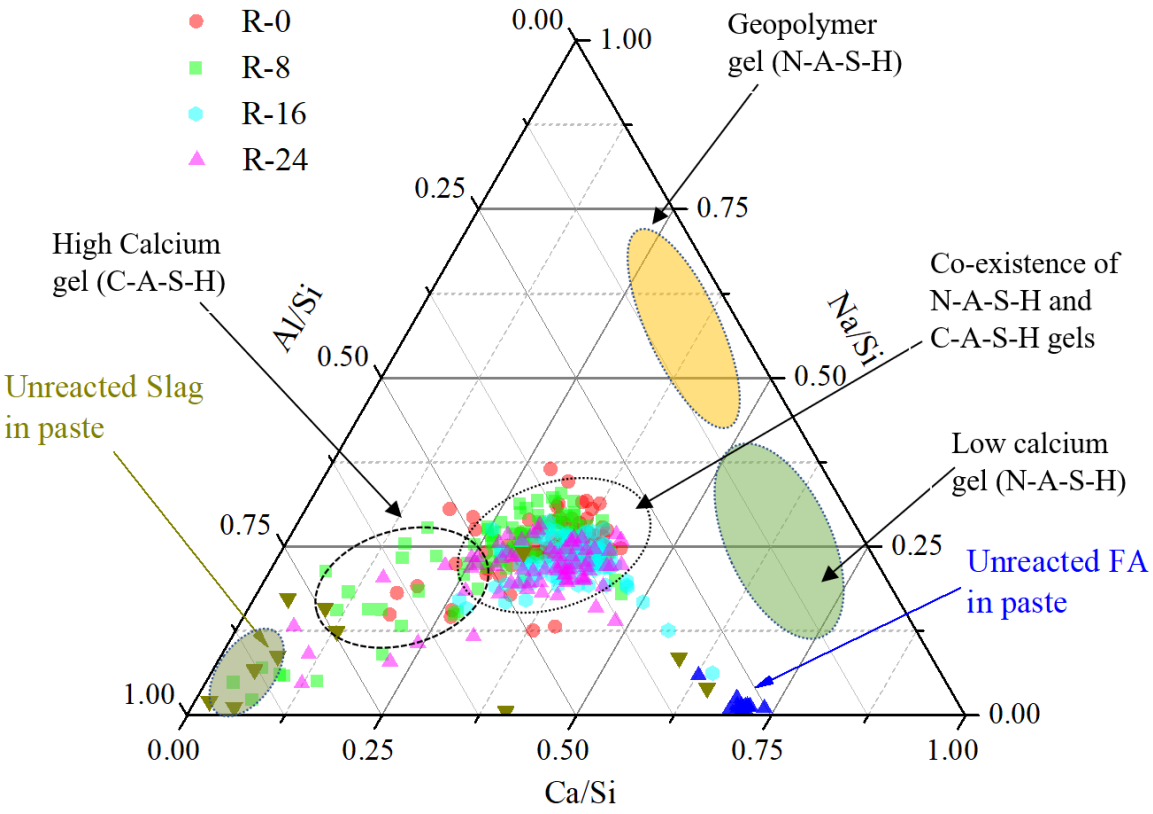

Fig. 8. Ternary diagram of AAFS pastes showing the molar ratios of Ca/Si, Na/Si and Al/Si

Table 5. Statistical analysis of AAFS pastes for the grouping of atomic ratios

Element Ratio	Paste ID	Mean	Min	1st quartile	Median	3rd quartile	Max	Tukey Test

								(Grouping)		
Ca/Si	R-0	0.37	0.07	0.32	0.39	0.44	0.53		B	C
	R-8	0.33	0.04	0.29	0.33	0.39	0.75			C
	R-16	0.44	0.14	0.37	0.43	0.49	1.12	A		
	R-24	0.39	0.04	0.33	0.39	0.48	0.65		B	
Na/Si	R-0	0.27	0.11	0.23	0.27	0.30	0.46	A		
	R-8	0.27	0.06	0.22	0.28	0.32	0.46	A		
	R-16	0.26	0.10	0.23	0.26	0.30	0.36	A	B	
	R-24	0.24	0.06	0.20	0.24	0.28	0.38		B	
Si/Al	R-0	2.52	1.08	2.09	2.41	2.69	6.92	A		
	R-8	1.95	0.23	1.67	2.06	2.35	3.95		B	
	R-16	2.28	1.47	1.98	2.21	2.37	5.27	A		
	R-24	2.21	0.40	1.82	2.11	2.36	8.82	A	B	
Na/Al	R-0	0.65	0.22	0.57	0.66	0.76	1.04	A		
	R-8	0.55	0.03	0.43	0.58	0.72	0.93		B	C
	R-16	0.58	0.21	0.50	0.59	0.67	0.84		B	
	R-24	0.50	0.05	0.42	0.51	0.60	0.84			C

3.4.2 SEM-EDS mapping of AAFS pastes

SEM-EDS mapping technique was used to further investigate the homogeneity of reaction products and distribution of major elements (Na, Ca, Al and Si). The results of mapping for the control paste (R-0) and the paste containing APCr as a 24% replacement of CSS are shown in Fig. 9 and Fig. 10 respectively. It can be observed that unreacted GGBS particles in the control paste R-0 were present in a higher amount than that of R-24. This supports the findings of SEM-EDS point analysis performed on the gel (section 3.4.1), where the Ca/Si ratio of gel in R-0 was lower (or unreacted GGBS was higher) than that of R-24, which means a lower amount of GGBS had reacted in the control AAFS paste (R-0) as compared to R-24 paste. The higher reaction degree of GGBS in R-24 can leads to the formation of a higher amount of alkali-activated gel (C-A-S-H) and calcium-rich cross-linked gel (C-(N)-A-S-H gel). The formation of cross-linked gel (C-N-A-S-H) was confirmed in the ternary diagram in all AAFS pastes and further validated by the homogenous distribution of gel elements Ca, Na, Si, and Al. The EDS mapping of R-8 and R-16, EDS spectrum, and elemental ratio of mapping images of all AAFS pastes are provided in the supplementary information (see Fig. A3-A7 and Table A1). Some unreacted phases of Mg, Fe (see Fig. A3-Fig. A7) and fly ash particles (observed from the correlation between Si and Al) are also observed in the mapping.

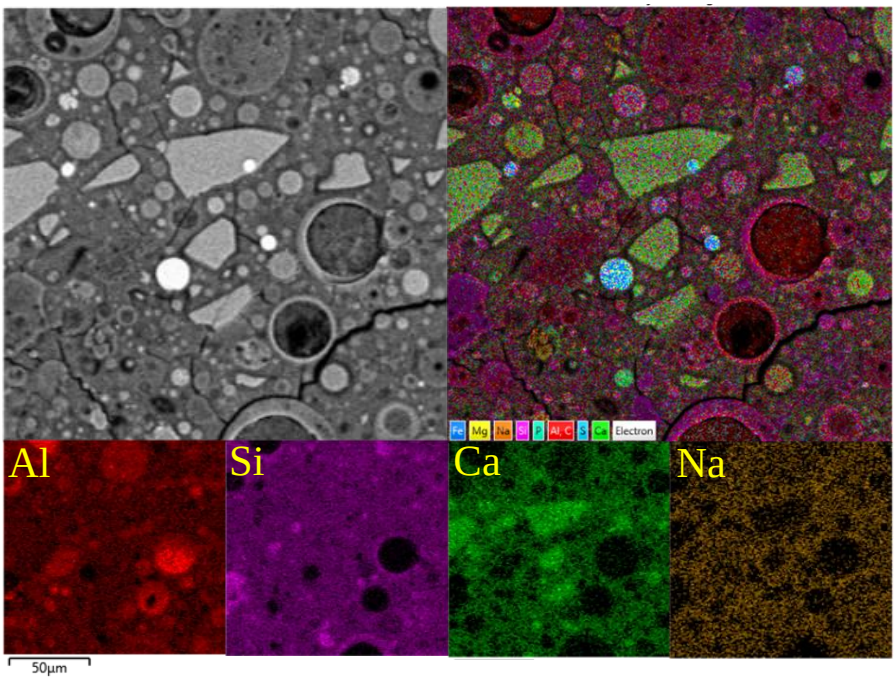

Fig. 9. SEM-EDS mapping of reaction products for R-0

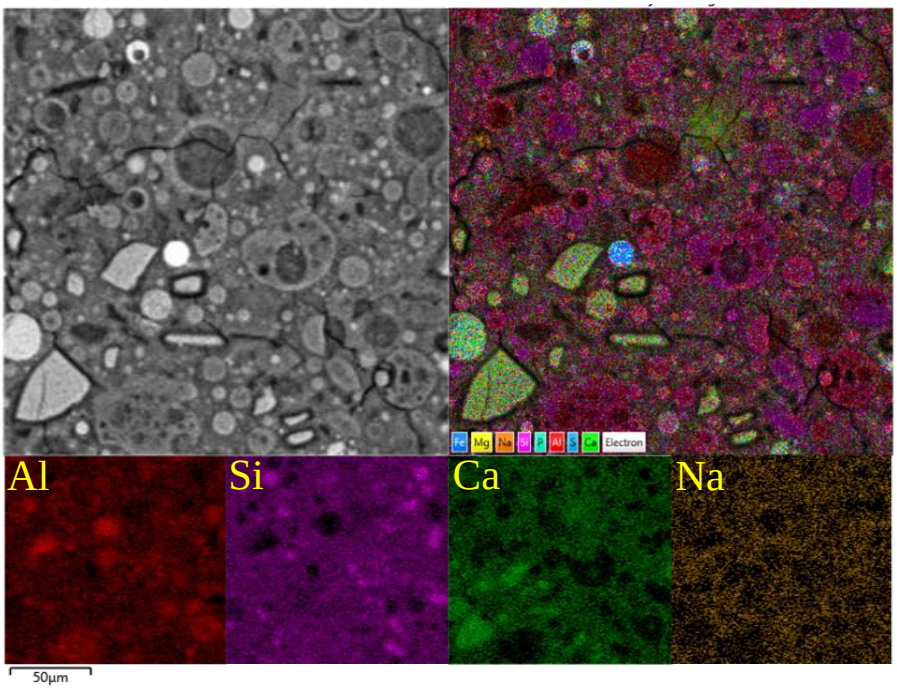

Fig. 10. SEM-EDS mapping of reaction products for R-24

3.5 FTIR analysis of AAFS pastes and study of dissolved gel products through spectral subtraction

3.5.1 FTIR analysis of raw materials and their residues

FTIR spectra of raw FA and residues of FA after water, HCl and SAM dissolution are plotted in Fig. 11a. The main band in raw FA appeared at 1027 cm^{-1}, which remained nearly the same at 1026 cm^{-1} after the SAM dissolution. The main band at the 1027 cm^{-1} was attributed to the asymmetric stretching vibration of Si-O-T (T = Si or Al) bond. After the HCl dissolution, the position of main band was (1027 cm^{-1}) shifted to slightly higher wavenumber of 1038 cm^{-1}, this is because HCl solution can change the surface area and microstructure of FA, which can cause dissolution of some of Al-rich phases and shift of band to slightly higher position. This implies that certain phases from the FA were dissolved after HCl treatment. The amount of FA dissolved after the SAM and HCl treatment was 13.5% and 26.7% respectively. The dissolution of FA due to the SAM and HCl treatment was higher as compared to the studies reported in the literature [14,55], this could be due to the different chemical composition and reactivity of FA from different sources. The influence of HCl dissolution was considered to be higher as compared to the SAM dissolution due to the higher amount of FA dissolution. The shift of main band in W-FA was due to the dissolution of alkaline phases into water. The influence of water dissolution was considered minimal and only 5% of FA was dissolved into the water. The presence of bands around 791, 775 and 756 cm^{-1} was associated with the quartz in FA [56]. The band around 446 cm^{-1} was due to presence of symmetric vibration frequencies of the Si–O bond [57].

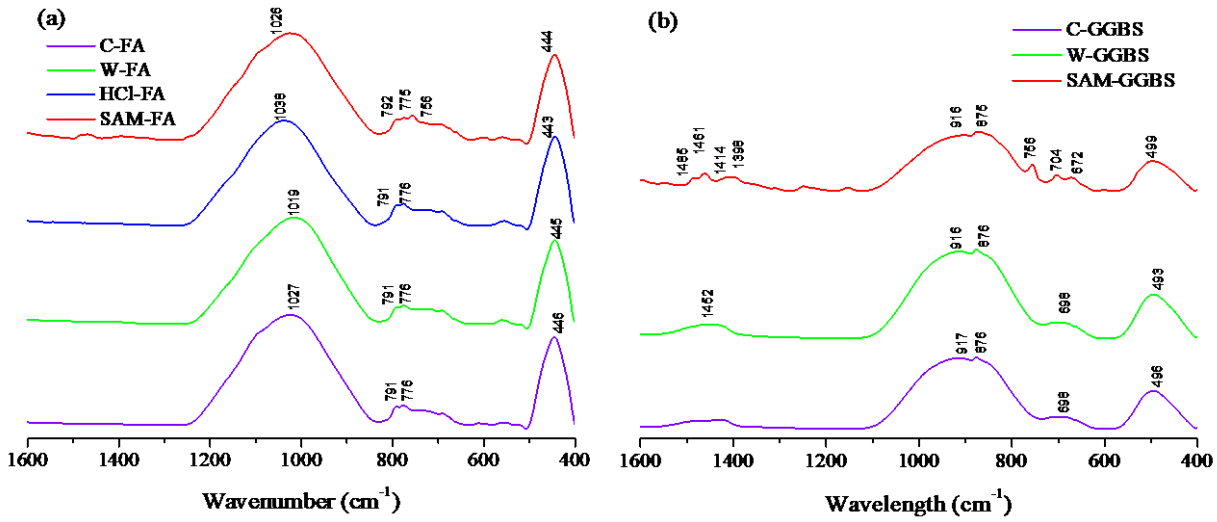

Fig. 11. FTIR spectra for (a) raw FA and its residues (b) raw slag and its residues after water, HCl and SAM dissolution

FTIR spectra of slag residues after water and SAM dissolution are shown in Fig 11b. Water dissolution did not change the band positions of slag residues and its effect was considered negligible. The main band in raw slag powder was located at peaks wavenumber of 917 and 876 cm^{-1} which was attributed to the asymmetric stretching vibration of Si–O–T [14]. The main band of slag appeared at a lower wavenumber as compared to FA, which was linked to the different natures of aluminosilicate phases in the two materials. The vibration spectrum of amorphous materials like slag was broad as compared to crystalline materials like FA. SAM-GGBS residues showed the appearance of some weak peaks (1398-1485 cm^{-1}) which were not observed in raw slag powder. The absorption bands in range of 1398-1485 belonged to anti-symmetric stretching vibration of O-C-O bond of CO_3^{2-}[58]. The band in raw slag powder at 496 cm^{-1} was due to bending vibration of Al-O bond [59]. The bands in the range of 672-756 cm^{-1} were associated with the presence and symmetric stretching vibration of Si-O-Si(Al) bonds [60]. Slag powder was completely dissolved in HCl solution which agreed with the previous studies. Hence, unreacted slag particles in alkali-activated paste would respond in a similar way to raw slag powder during HCl dissolution.

3.5.2 FTIR analysis of original AAFS pastes

The FTIR spectra of original AAFS pastes powders are provided in Fig. 12. The main band in case of all mixtures was concentrated around the 968-970 cm^{-1} and was associated with the asymmetric stretching

vibration of Si-O-T bond (T = Si or Al). This band was shifted from higher wavenumber (1027 cm^{-1}, in raw FA) to lower wavenumber (970 cm^{-1}, in AAFS pastes). The shifting of band occurred due to the reaction of precursors to form the geopolymer/alkali-activated gels (M-A-S-H, M= Na or Ca). As the reaction proceeded, substitution of Si with Al was increased due to lower bond force of Si-O-Al than that of Si-O-Si, and original structure of the aluminosilicate precursors was significantly depolymerized. The Si/Al ratio of tetrahedral Si sites was continuously decreased during the reaction process to form the alkali-activated gels. These sites were initially surrounded by the Al atoms and after dissolution of Al from precursors during the reaction process, M-A-S-H gel network was formed as a larger number of tetrahedrally linked Al atoms and Si atoms were bridged by oxygen atoms [61,62]. This network structure of M-A-S-H resulted in the shift of band (Si-O-T) to a lower wavenumber. The main band of all mixtures fell between the shoulders at 1123 and 877 cm^{-1} with peaks concentrated around 968-970 cm^{-1}. It is important to mention that main bands were present in between the wavenumbers 1020 cm^{-1} and 950 cm^{-1} which are associated with the N-A-S-H and C-A-S-H gels respectively. This means that reaction products at wavenumber 968-970 cm^{-1} were comprised of cross-linked gels and were richer in Ca phases (C-(N)-A-S-H). The main band for the control paste (R-0) was located at 970 cm^{-1}, which was slightly shifted to the lower wavenumber of 969 cm^{-1} and 968 cm^{-1} for R-8 and R-24 respectively. This indicates that a slightly higher amount of polymerization of reaction products took place in R-8 and R-24 as compared to R-0. This could also explain the slightly higher strength of R-8 and R-24 as compared to R-0 as discussed in section 3.1. Formation of slightly higher amount of reaction products in the APCr-based pastes could be due to the higher alkalinity of mixtures. The higher alkalinity could help to dissolve the precursors more easily and lead to formation of higher amount of reaction products. At a high silicate modulus of 0.91 (R-0), more dissolved Si was available from the sodium silicate and also a higher amount of Ca, Si and Al from slag which could form more reaction products at an early stage. When sodium silicate was replaced by APCr, the silicate modulus (Si/Al) was slightly decreased to 0.74 (R-24), which in turn increased the alkalinity of mixture. The higher alkalinity could further increase the reaction of both fly ash and slag thus accelerating the dissolution of alumina and silica in mixtures that had a slightly low silicate modulus. Gao et al., [49] also reported that

for the fixed FA/GGBS, a decrease in silicate modulus resulted in a higher amount of reaction products. However, variation in the amount and nature of reaction products was marginal due to insignificant variation in the silicate modulus and alkalinity. The carbonation of AAFS pastes was revealed by the band present at 1413 cm^{-1} which occurred due to asymmetric stretching of O-C-O bond of CO_3^{2-}.

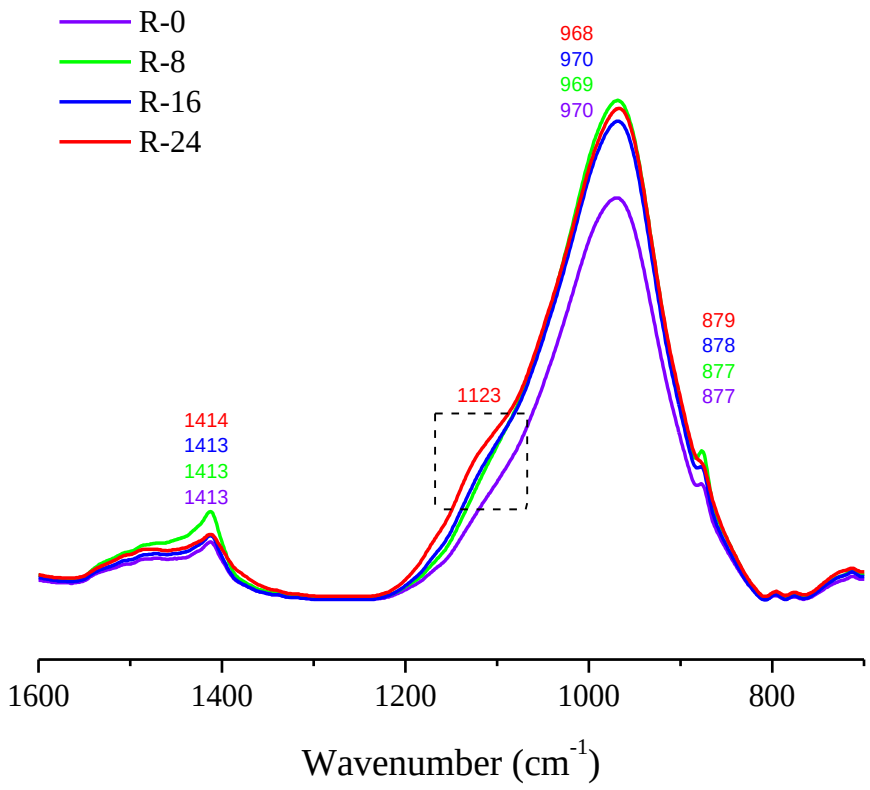

Fig. 12. FTIR spectra of original AAFS pastes powders

3.5.3 FTIR analysis of residues after HCl, SAM and water dissolution

Selective dissolution on all AAFS pastes powders was performed by HCl and SAM treatment. The influence of water dissolution was also studied. The results are plotted in Fig. 13. The main band (Si-O-T bond at 968-970 cm^{-1}) in all AAFS pastes was shifted to a slightly higher wavenumber (978-983 cm^{-1}) under the water dissolution. The shifting of main band to higher wavenumber was the indication of leaching out of alkalis from the non-bridging oxygen sites (Si-O-Na) and dissolution of Al(IV) sites in small quantities, which resulted in the reduction of Si-O-Al bonds. The presence of Al in M-A-S-H network structure was

observed via tetrahedral coordination and hence a negative net charge was present due to the substitution of Si^{-4} with Al^{+3} which was balanced by the Na^{+} ions from the activator (sodium silicate or APCr) [63]. The negative charge (on Al atoms) in M-A-S-H gel could also be neutralized by the extra-framework Al atoms (e.g. Al(IV) species) when sufficient quantities of Al are present. Therefore, distortion in M-A-S-H gel structure was induced and main band (Si-O-T) was shifted to a higher wavenumber. During this process, some of the Al in tetrahedral were converted to non-tetrahedral bonding of Si [61,64].

After the HCl treatment of AAFS pastes, main band was shifted to significantly higher wavenumber (1050-1056 cm^{-1}). When AAFS paste powder was treated with the HCl, geopolymer gel, zeolites and unreacted slag particles were dissolved, however a significantly lower proportion of FA was dissolved. Calcium carbonate was also dissolved and calcium silicate hydrates were also affected as HCl treatment can remove the calcium by leaving the silica gel behind. Hence, HCl treated residues of AAFS pastes primarily were composed of unreacted fly ash. It can be observed that carbonation band around 1413 cm^{-1} disappeared in all pastes after HCl treatment and bands around 777 and 793 cm^{-1} appeared (associated with crystalline quartz presence in FA). The FTIR spectra of AAFS pastes residues after HCl treatment matched with the FTIR spectra of raw FA (Fig. 11a).

FTIR spectra of AAFS pastes residues after SAM treatment showed significant changes as compared to the original spectra (Fig. 13). Main band in the original spectra moved to a higher wavenumber (1034 cm^{-1}) after SAM treatment of AAFS pastes powders with a new shoulder appearing around 1140-1145 cm^{-1}. SAM solution could dissolve the calcium silicate, calcium hydroxide and calcium oxides however it did not dissolve calcium carbonate. The presence of carbonation peaks (1394-1464 cm^{-1}) can be observed in the AAFS pastes SAM residues spectra. A small proportion of FA and slag is dissolved in SAM solution. The influence of SAM on FA and slag spectrum was negligible as observed in Fig. 11. It has been also reported that geopolymer gel (N-A-S-H) is not dissolved by SAM treatment. Hence, a shift in the main band was primarily associated with the dissolution of calcium-rich alkali-activated gel (C-A-S-H) [65,66]. Appearance of a weak band around 1140-1145 was associated with the stretching vibration of Si-OH bond

present in geopolymer gel as it was insoluble in SAM solution. Another absorption band around 1087 cm^{-1} was due to plane vibration of Si-OH tetrahedron [67]. The band around 1123 cm^{-1} appeared in R-24 and was related to the asymmetric stretching vibration of Si-O bond (linked to Q^3 sites).

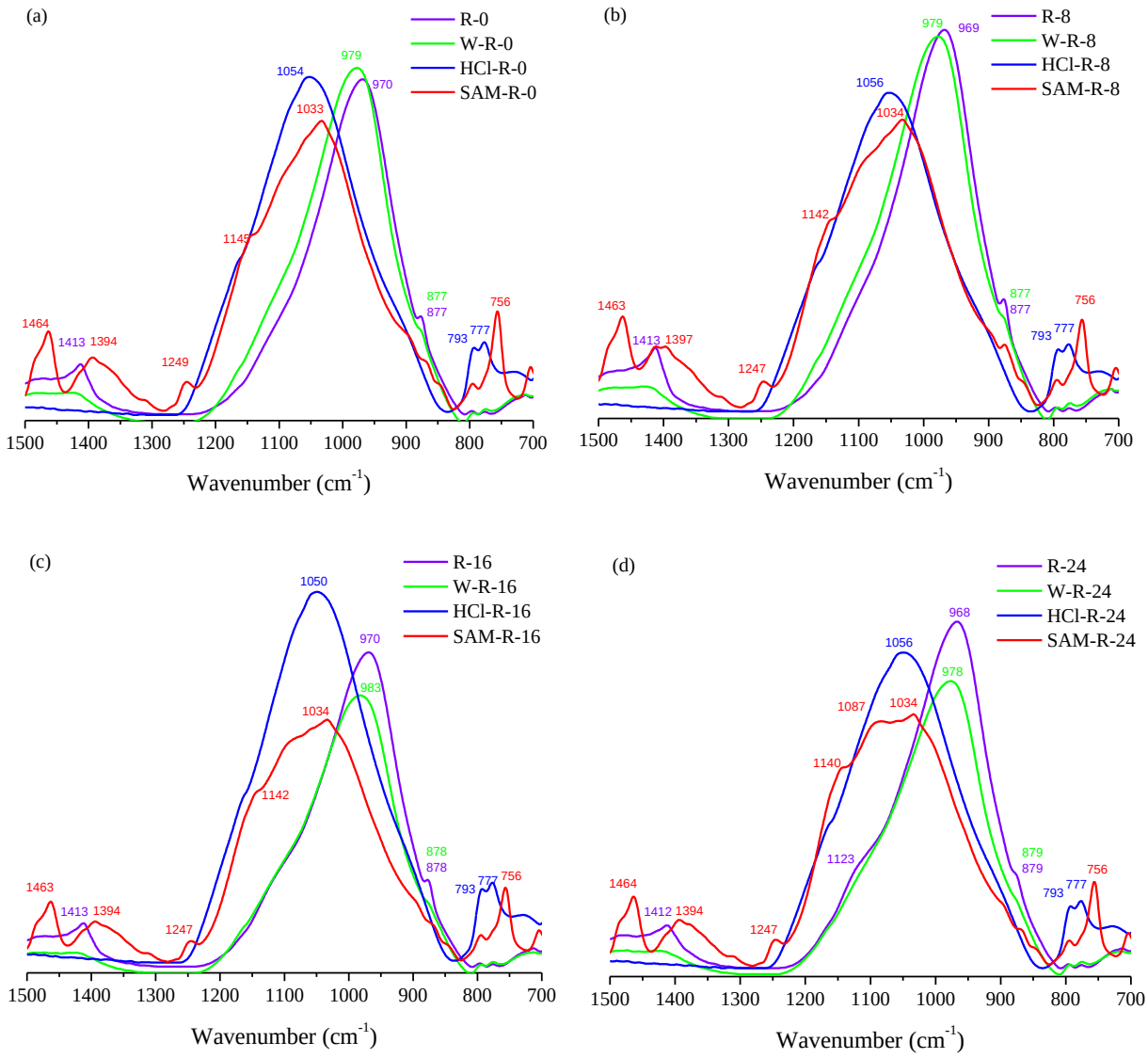

Fig. 13. FTIR spectra of insoluble AAFS paste residues after Water, HCl and SAM dissolution for (a) R-0, (b) R-8, (c) R-16 and (d) R-24

3.5.4 FTIR spectra of dissolved phases determined through spectral subtraction

The spectral subtraction of all cement paste was performed to study the reaction products which were dissolved due to HCl and SAM treatment. The subtracted spectra were obtained by subtracting the residue spectra from original spectra of each paste using OMNIC software and are shown in Fig. 14. The spectra

were plotted in the range of 700-1500 cm^{-1} to study the dissolution of main reaction products. It is important to mention that spectra of dissolved reaction products in all AAFS pastes showed the main band concentrated around the 965-970 cm^{-1}, which is associated with the asymmetric vibration stretching vibration of tetrahedral Si or Al bonds (Si-O-Si/Al). Position of the main band is slightly higher than the main band of alkali-activated calcium-rich gel (C-A-S-H, 950 cm^{-1}) and lower than that of geopolymer gel (N-A-S-H, 1020 cm^{-1}). This proves that reaction products in all pastes were mainly in the form of co-existence of both types of gels (C-A-S-H and N-A-S-H gels), however, reaction products were more dominant in calcium-rich phases (C-(N)-A-S-H) as wavenumber of reaction products is closely inclined to main band of alkali-activated gel [68–71]. It can be observed that with the increase in replacement of sodium silicate by APCr, the difference between the original and dissolved spectra was gradually increased and a new peak starts to appear around the 1123 cm^{-1} which became more evident in the pastes containing 16% and 24% APCr. The weak peak around 1123 cm^{-1} indicates the dissolution of silica-rich reaction products containing some amount of calcium and alkali [14]. However, smaller intensity of band around 1123 cm^{-1} as compared to the main band shows that quantity of silica-rich gel with calcium was low. Therefore, it is postulated that as amount of APCr was increased to 16% and 24%, a slightly higher amount of calcium-based silica-rich gel (C-A-S-H) was formed due to the appearance of band around 1123 cm^{-1}. The previous study reported that blends of slag and fly ash can produce the C-A-S-H and N-A-S-H or cross-linked C-N-A-S-H gel which can further improve the mechanical properties of pastes [71]. As HCl could also dissolve calcium-based gel (C-S-H and C-A-S-H) along with the geopolymer gel, whereas SAM mainly dissolved the C-A-S-H gel, the presence of geopolymer gel (N-A-S-H) was over-estimated from the HCl dissolved spectra. Hence, it can be concluded that reaction products majorly consisted of calcium-rich alkali-activated gel (C-A-S-H) phases. The peaks around 1412 cm^{-1} and 877 cm^{-1} which were present in original spectra but not in residues spectra, appeared in the subtracted spectra showing that carbonation species can exhibit the complete or very low solubility in the HCl and SAM solution respectively.

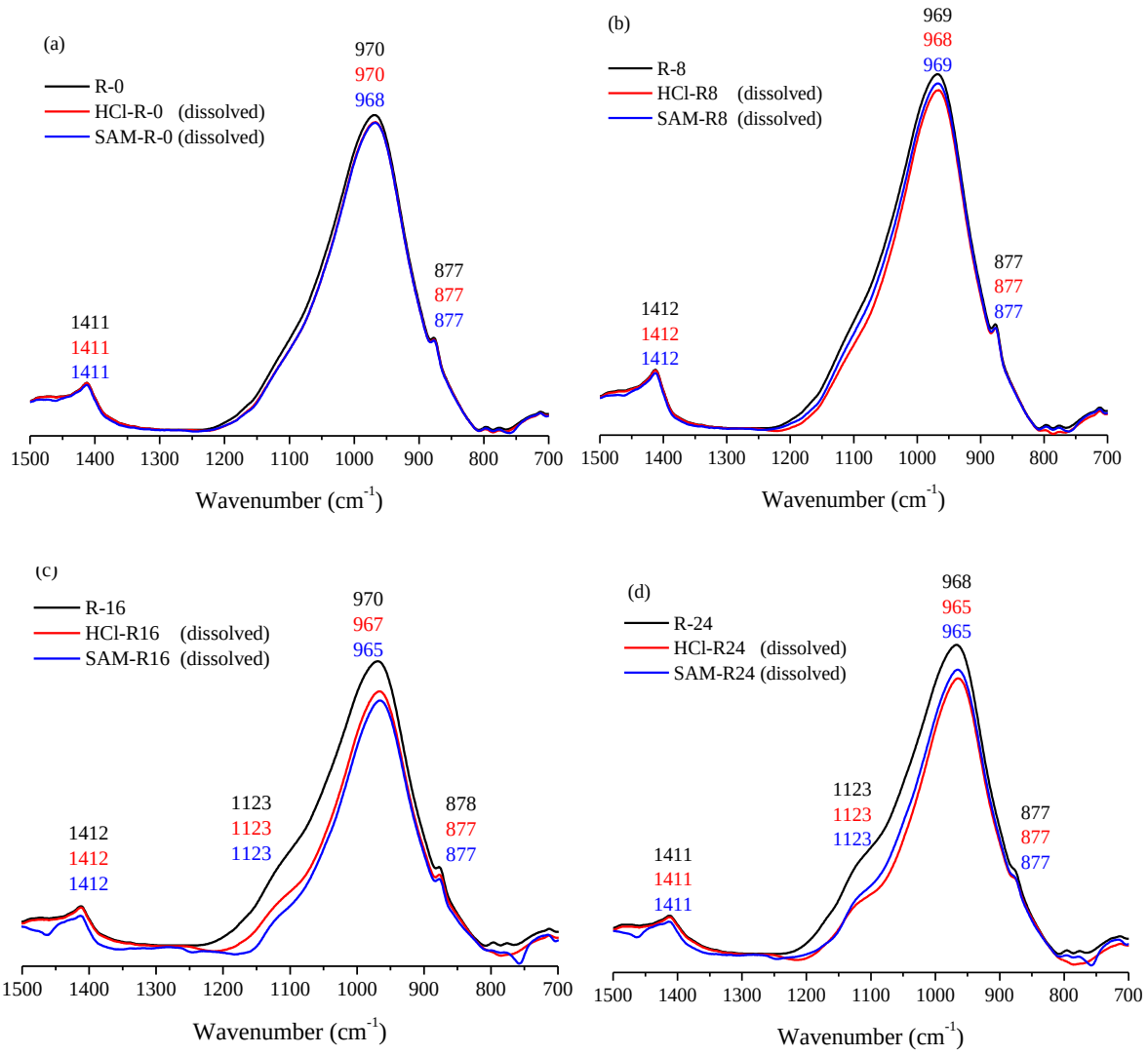

Fig. 14. Subtraction spectra of dissolved phases for (a) control paste without APCr, R-0, (b) paste containing 8% APCr, R-8, (c) paste containing 16% APCr, R-16 and (d) paste containing 24% APCr, R-24

3.6 Quantification of reacted and unreacted phases in AAFS pastes

Several BSE images were captured from the polished specimen of each AAFS pastes after 28 days of curing and processed for the image analysis. The use of image analysis to quantify the phases in hydrated cement paste has been reported in the literature [72,73]. In this study, BSE image analysis was performed to quantify the four major phases observed in reaction products namely gel phases (N-A-S-H, C-A-S-H, C-N-A-S-H) and unreacted phases (FA, GGBS, and Fe). These four phases were separated due to their different grey scale level via image segmentation of BSE images. For each AAFS paste, five BSE images were

selected at different locations to determine the average of each phase. The image segmentation of different phases for the AAFS paste (R-16) and a composite color image is shown in Fig. 15. The segmentation of phases was further confirmed by the SEM-EDS points analysis. The quantitative analysis of each phase for all AAFS pastes is provided in Fig. 16. The amount of gel phases did not show significant variation among the different pastes. The amount of reaction products (gel phases) was 60.8%, 60.4%, 60.1% and 60.6% for R-0, R-8, R-16 and R-24 respectively. This validates the efficacy of APCr as a replacement for CSS. Moreover, these findings also confirmed the results of compressive strength of mixture at 28 days, where all AAFS pastes showed equivalent compressive strength in the range of 61.5 to 63.5 MPa. The percentage of unreacted phase of FA in control paste was 28.2% which was lower than that of R-8 (32%), R-16 (31.5%) and R-24 (30.5%). Hence, it is postulated that reactivity of FA was slightly decreased due to addition of APCr however a slightly higher amount of GGBS reacted in the presence of APCr. The amount of unreacted GGBS was 10% in R-0 and was the highest among all pastes. A minor quantity of unreacted Fe phases in range of 0.5-1.7% was also observed in AAFS pastes.

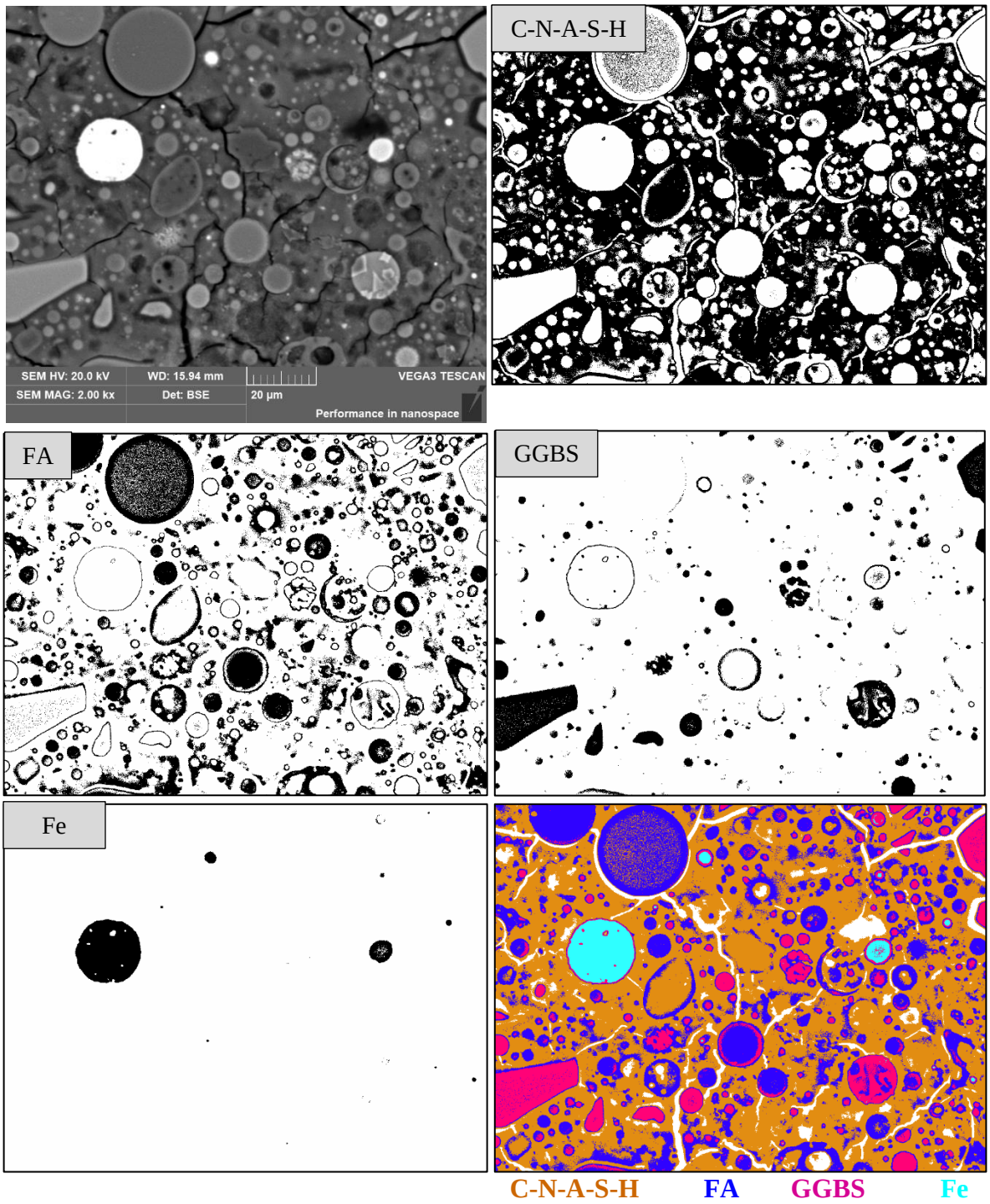

Fig. 15. Phase segmentation of different phases of BSE images through image analysis for R-16

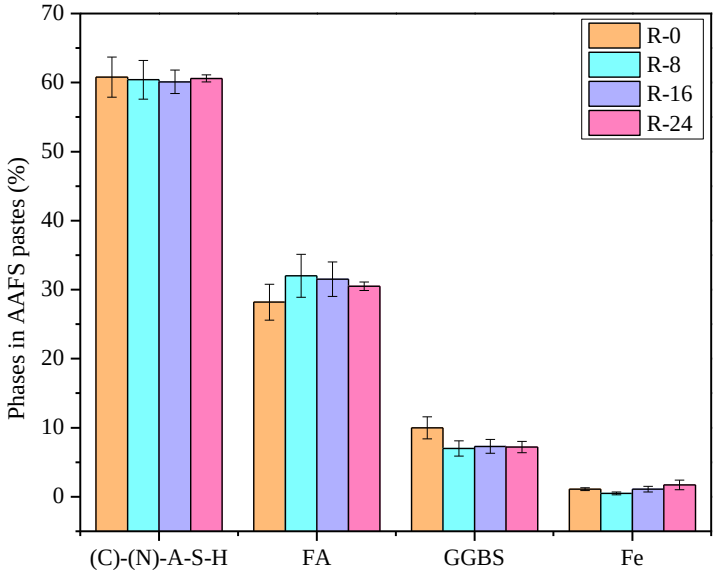

Fig. 16. Quantification of phases through image analysis

3.7 Micromechanical study of AAFS pastes gel composition

The nanoindentation test can be used to characterize the mechanical properties of reaction products and can provide the data for statistical analysis [74,75]. Both Alkali-activated gel (C-A-S-H) and geopolymer gel (N-A-S-H) can contain some amounts of Na and Ca, which make its difficult to quantify them based on SEM-EDS analysis [76]. However, their micromechanical properties (e.g. Elastic modulus and hardness) are different and thus can be quantified using the nanoindentation. In this study, grid nanoindentation was performed on all pastes. It has been reported that unreacted phases (FA, GGBS, Fe) have higher elastic modulus as compared to reaction products. The micromechanical properties of AAFS pastes are converted into mapping contours and are plotted in Fig. 17 on grid dimensions of 100 × 100 µm. The contours maps are separated into two main categories i.e., reaction products and unreacted particles. The unreacted particles cover the contours with higher modulus and are shown with cyan and red colors (e.g. E > 50 GPa). The unreacted GGBS falls in the range of 50-75 GPa. Some Al-rich FA particles also fall in this range. Most of the FA particles (Si-rich FA, Fe-rich FA and Ca-rich FA) and unreacted Fe particles fall in the range of E > 75 GPA [77]. The formation of different types of gel phases (N-A-S-H, C-N-A-S-H, and C-A-S-H) are reported to have lower elastic modulus as compared to unreacted phases and mostly fall under the elastic modulus of 50 GPa [74,75,77–80].

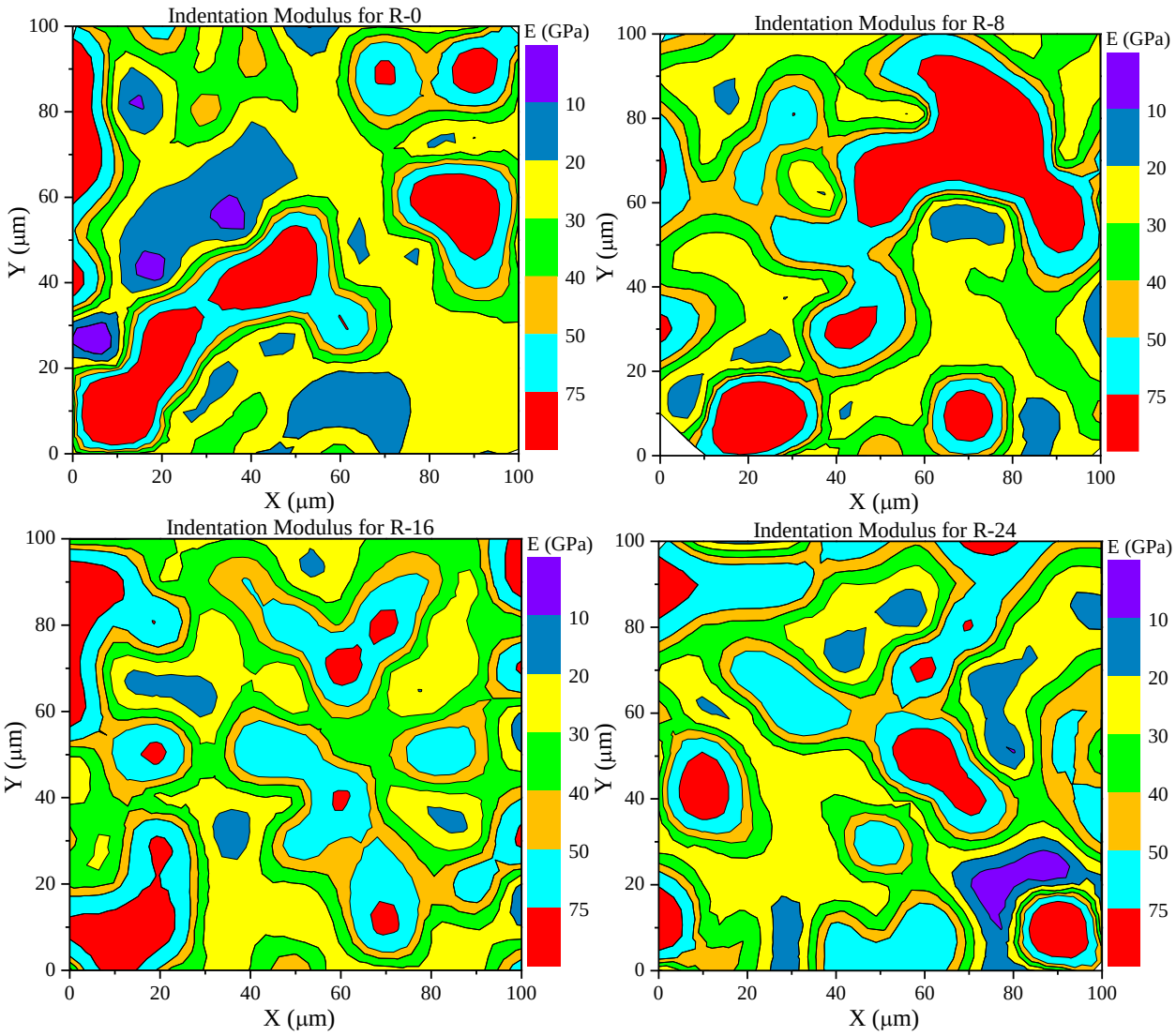

Fig. 17. Contour map of Elastic modulus of AAFS pastes test at 28 days curing age

The existence of different mechanical states (different elastic moduli) of same type of gel has been reported [75]. Studies have shown that for alkali-activated hybrid FA-GGBS pastes, there is a simultaneous presence of N-A-S-H, C-N-A-S-H, and C-A-S-H. The elastic modulus of N-A-S-H geopolymer gel is reported to be < 20 GPa [78,80]. Cross-linked gel (C-N-A-S-H) shows a relatively higher elastic modulus as compared to geopolymer gel and hence falls in the range of 20-30 GPa [77]. The highest elastics modulus among the reaction products is observed in alkali-activated gel (C-A-S-H) whose modulus varies from 30 to 50 GPa [75]. The hardness vs elastics modulus plots for the different pastes are plotted in Fig. 18. The elastics

modulus of pastes can be related to the stiffness and the hardness can be related to the strength of paste. The strength of N-A-S-H gel was lower as compared to cross-linked gel (C-N-A-S-H) and calcium-rich gel (C-A-S-H) in all pastes (with H ≤ 1 GPa). The cross-linked gel (C-N-A-S-H) had relatively higher strength than the N-A-S-H (H ≤ 2 GPa) but lower than that of C-A-S-H, which shows wide dispersion of hardness values. The hardness of C-A-S-H gel was below 3 GPa in R-0 and R-16 pastes and ≤2.5 GPa in R-8 paste. For the R-24 paste, a wide range of distribution of C-A-S-H was observed reaching the maximum hardness of 5.5 GPa. These results support the high Ca/Si ratios for R-0, R-16, and R-24 pastes as compared to R-8 as observed in SEM-EDS analysis. Moreover, a significant amount of partially reacted GGBS was also found in R-24 paste as it shows a similar hardness and elastic modulus.

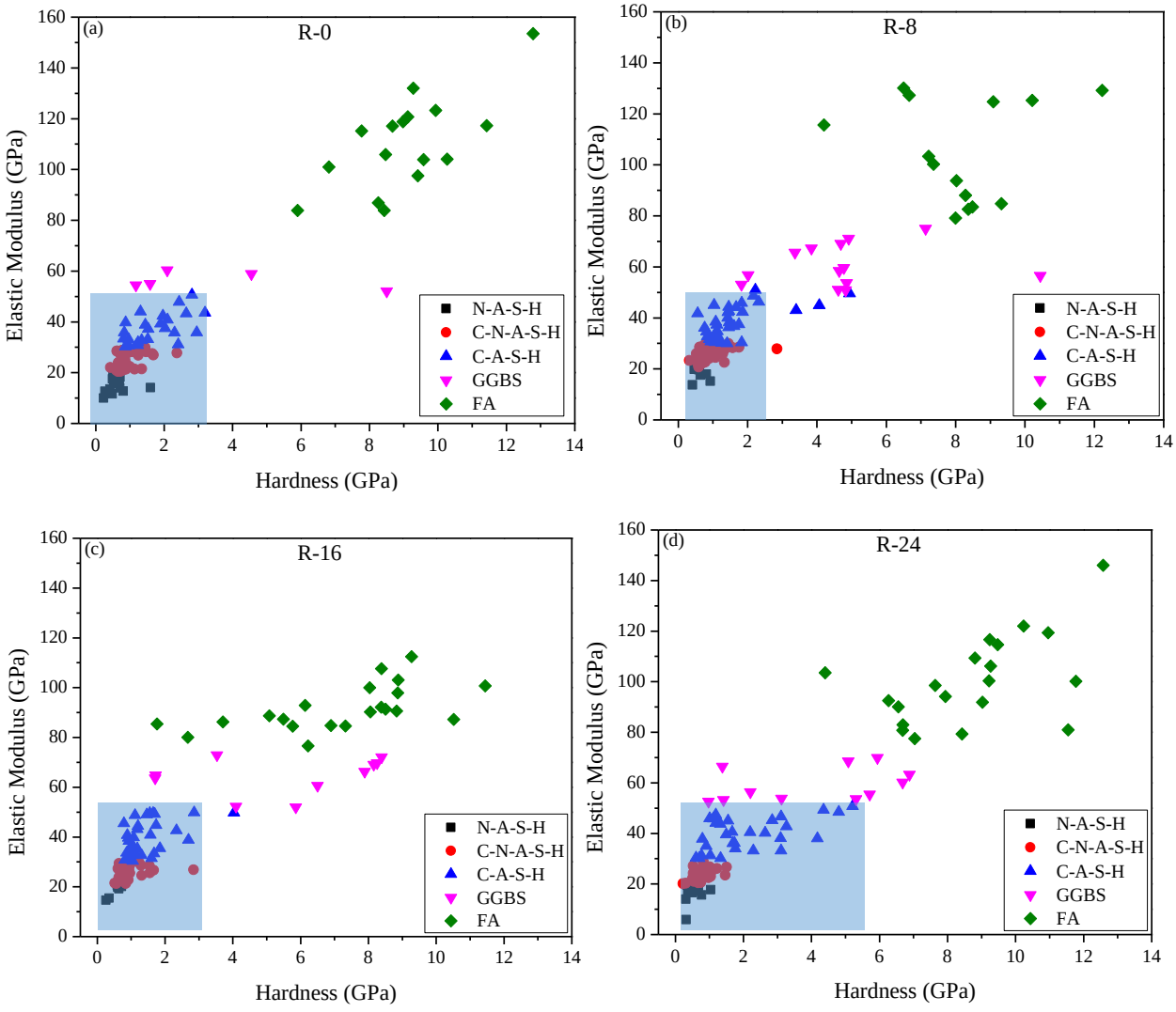

Fig. 18. Plots of Hardness vs Elastic modulus of AAFS pastes for (a) R-0, (b) R-8, (c) R-16 and (d) R-24

The contours of mapping areas were quantitively analyzed by the imaging analysis software to calculate reaction products and unreacted phases. The results of quantitative analysis of contours plots performed by image analysis are shown in Fig. 19. The total amount of reaction products were lowest in R-8 paste which were 60%. The reaction products in the APCr-AAFS pastes R-0, R-16, and R-24 were in a similar range and varied from 64.2 to 66.4% (Fig. 19a). Based on the elastic modulus (N-A-S-H < C-N-A-S-H < C-A-S-H), the reaction products are further categorized into the N-A-S-H, C-N-A-S-H, and C-A-S-H as shown in Fig. 19b. The amount of C-A-S-H gel was higher as compared to C-N-A-S-H and N-A-S-H in all AAFS pastes. The amount of cross-linked gel (C-N-A-S-H) was gradually decreased with the replacement of CSS, which showed that the presence of CSS can facilitate the cross-linked gel in hybrid FA-GGBS materials. The highest amount of C-A-S-H gel (41.2%) was present in R-16 paste, followed by R-24 (33.8%), R-8 (33.2%), and R-0 (28.8%). SEM-EDS analysis also showed that R-16 had the highest amount of C-A-S-H gel as compared to other pastes (Ca/Si ratio of 0.49 (3rd quartile) shown in Table 5). It is important to mention that C-A-S-H gel in ACPr-AAFS pastes showed superior homogeneity and connectivity as compared to control paste (see Fig. 17, green and orange contours).

On contrary to SEM-EDS analysis and selective dissolution, a lower amount of unreacted GGBS was observed in control cement paste (R-0) as compared to APCr-AAFS pastes. This difference could be due to the presence of some Fe-rich and Al-rich FA particles in the modulus range selected for GGBS (50-75 GPA) as reported in the literature [77]. However, the total amount of unreacted phases (GGBS, FA, and Fe) from the nanoindentation (Fig. 19a) and SEM-EDS image analysis (Fig.16) showed minor variation. A slight difference in the reaction products and unreacted phases from the nanoindentation test can be associated with the presence of different nature of phases at selected locations in AAFS pastes.

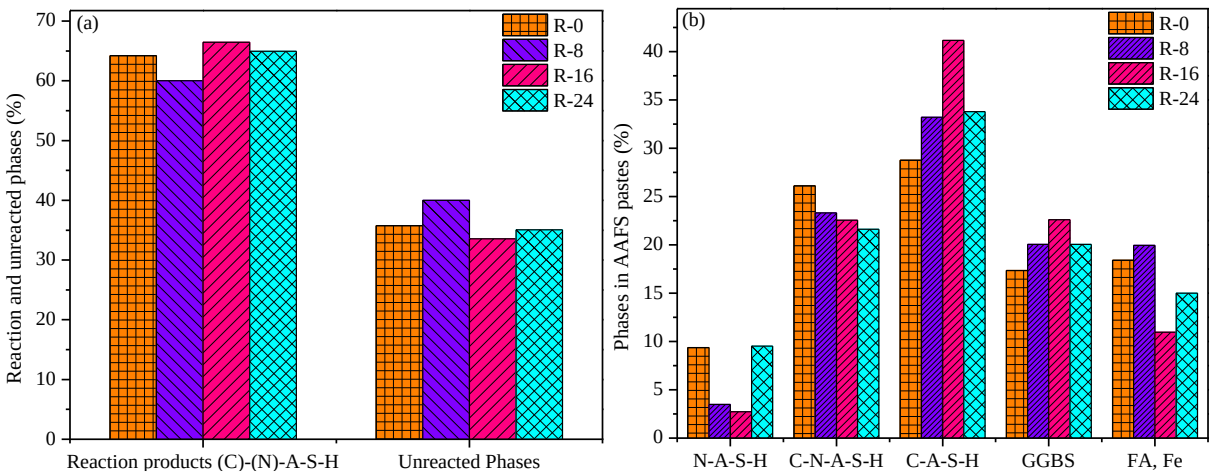

Fig. 19. Quantitative analysis of reaction products analyzed by nanoindentation

3.8 Study of reaction products by thermogravimetric analysis (TGA)

TGA and DTG analysis was employed to characterize the reaction products of AAFS pastes. TGA analysis of AAFS pastes at an early age of 7 days is shown in Fig. 20a. As identified from the SEM-EDS, selective dissolution, and nanoindentation, primary products in the AAFS pastes are N-A-S-H, C-N-A-S-H, and C-A-S-H gels, the loss of mass at different temperatures can be associated with the presence of these reaction products. At the age of 7 days, the first but major mass loss peak occurred at 50°C, whereas the second peak occurred around 760°C. The loss in mass at a lower temperature was attributed to dehydration of physically bound water up to 150°C [48,81,82]. The rate of mass loss was slowed down beyond 150°C. At an early age, a higher loss in mass up to 150°C was observed for the control paste (R-0), which was 9.1% (Fig. 20e). The mass loss was gradually reduced when CSS was replaced by APCr. The water from the geopolymer gel (N-A-S-H) was removed at 300°C, whereas calcium-rich gel (C-A-S-H) dehydrated between 300-600°C. The mass loss due to reaction products normally occurs in the temperature range of 550-600°C, hence mass loss up to 600°C can be attributed to the total amount of reaction products. At the age of 7 days, a higher mass loss was observed in the control paste upto 600°C as compared to APCr-based pastes. This shows that a higher amount of reaction products were formed in the control paste at an early age. The loss in mass beyond 600°C is primarily attributed to the decomposition of calcite ($CaCO_3$) [48]. At the age of 28 days, TGA curves showed opposite behavior, and sample R-24 showed the highest mass

loss up to 600°C (Fig. 20c). The first major peak was also shifted to a higher temperature of 90°C. Another broad peak appeared in the range of 250-400°C (Fig. 20d) associated with the dehydration of N-A-S-H [48]. The increase in amount of N-A-S-H gel was observed at 28 days as compared to 7 days. The highest mass loss in R-24 up to 600°C showed that more amount of reaction products was formed as compared to control paste (R-0). Reaction products in R-8 and R-16 samples were also higher as compared to R-0. These results validated that the reaction process was slow during an early age (up to 7 days) due to the low reactivity of APCr. At a later age, reaction due to the inclusion of APCr slowly and gradually progressed, which contributed to a higher strength gain rate as observed in the compressive strength section of AAFS pastes.

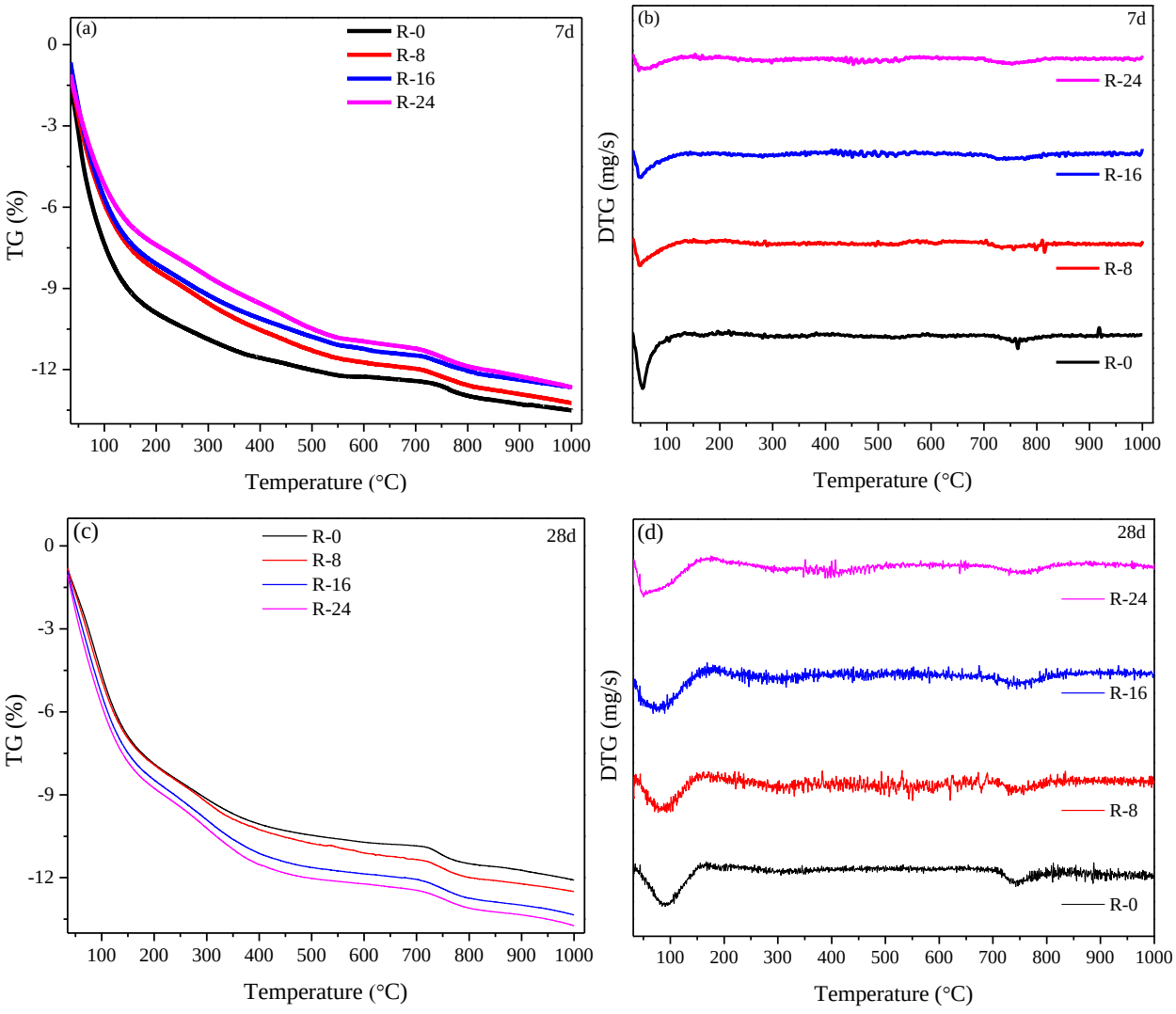

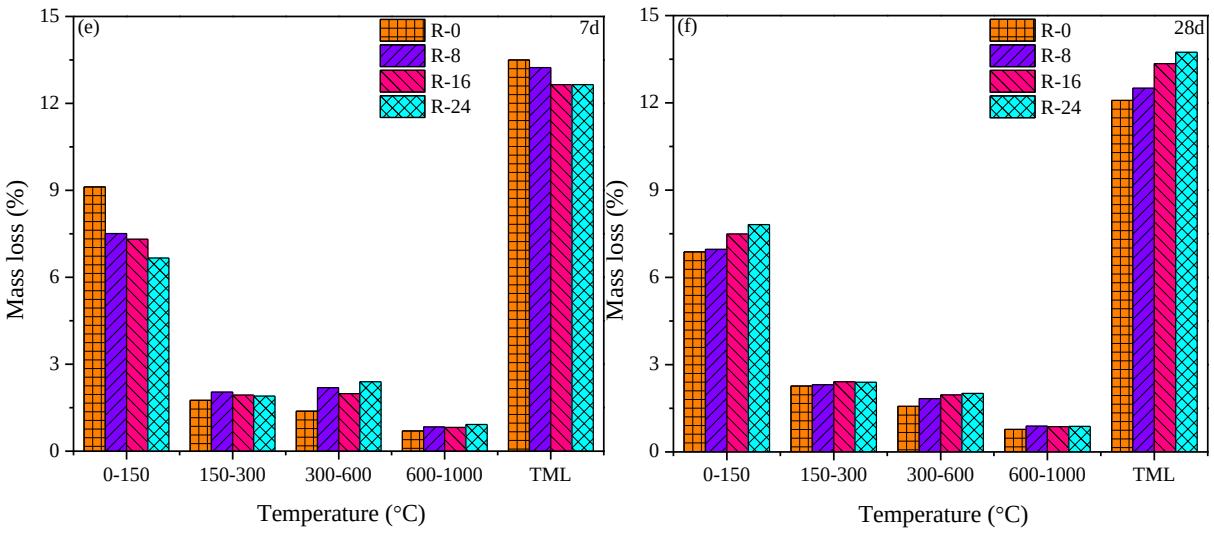

Figure 20. Thermogravimetric analysis of AAFS pastes at 7 days and 28 days

4 Conclusions

In this research, hybrid AAFS pastes were prepared by studying the feasibility of using APCr as a partial replacement of CSS activator at different replacement levels of 8, 16, and 24% by mass. A comprehensive study covering the wide range of mechanical, microstructure, heat evolution, and micromechanical techniques were performed for the characterization of gels composition of AAFS pastes. Based on experimental results, conclusions are presented below.

1. The rate of strength gain was highest for the control cement paste (R-0) as compared to APCr-AAFS pastes during an early age due to the rapid dissolution of CSS activator. With the increase in curing age, APCr-AAFS pastes closed the strength gap and achieved the compressive strength equivalent to control cement paste.
2. The heat of hydration test validated the development of compressive strength results. The heat flow rate was highest at an early age for control AAFS paste due to rapid dissolution of CSS, precursors, and early precipitation of reaction products. However, APCr based activator reacted slowly with the progress of time and heat of hydration of APCr-AAFS pastes was similar or slightly higher than that of control AAFS paste at 14 days.

3. TGA-DTG results also validated the strength results as higher mass loss in APCr-AAFS pastes was observed at 28 days than the control paste, reflecting that a higher amount of reaction products were formed in APCr-AAFS pastes.
4. MIP results concluded that the use of APCr could change the pore size distribution of AAFS pastes. The amount of gel pores associated with the reaction products gradually increased from 14.9% to 31.4% as CSS was partially replaced by APCr, however, a slight increase in large size pores (>100 nm) was also observed.
5. SEM-EDS mapping revealed that major elements were homogeneously distributed in all AAFS pastes. The pastes containing higher amount of APCr (16% and 24% APCr) also showed the formation of higher amount of calcium-rich gel as compared to control cement paste. Ternary diagram showed that reaction products mainly consisted of cross-linked gel (C-N-A-S-H) and calcium-rich alkali-activated gel (C-A-S-H).
6. The image analysis, and nanoindentation micromechanical analysis showed a similar amount of total reaction products (N-A-S-H, C-N-A-S-H, C-A-S-H) in all matrices, which were in the range of 60-66% of total paste volume. The gel was mainly composed of cross-linked gel (C-N-A-S-H) and calcium-rich gel (C-A-S-H) as observed from the micromechanical analysis.
7. The presence of cross-linked gel (C-N-A-S-H) was confirmed by the FTIR results as the main band of reaction product (965-970 cm^{-1}) was present between the main band of geopolymer gel (1020 cm^{-1}) and calcium-rich alkali-activated gel (950 cm^{-1}). The results of this study provide a useful insight to determine the gel composition of alkali activator materials and are expected to contribute in finding the alternative alkaline activator for the preparation of AAMs.

Acknowledgments

The authors would like to acknowledge the financial support received from NSFC/RGC Joint Research Scheme (N_PolyU542/20), Hong Kong RGC General Research Fund (No. 15223120), The Hong Kong Polytechnic University through the Research Institute for Sustainable Urban Development (No.1-BBWE).

References:

[1] B.C. McLellan, R.P. Williams, J. Lay, A. van Riessen, G.D. Corder, Costs and carbon emissions for geopolymer pastes in comparison to ordinary portland cement, Journal of Cleaner Production. 19 (2011) 1080–1090. https://doi.org/https://doi.org/10.1016/j.jclepro.2011.02.010.

[2] A. Passuello, E.D. Rodríguez, E. Hirt, M. Longhi, S.A. Bernal, J.L. Provis, A.P. Kirchheim, Evaluation of the potential improvement in the environmental footprint of geopolymers using waste-derived activators, Journal of Cleaner Production. 166 (2017) 680–689. https://doi.org/https://doi.org/10.1016/j.jclepro.2017.08.007.

[3] M.R. Ahmad, B. Chen, S.F.A. Shah, Influence of different admixtures on the mechanical and durability properties of one-part alkali-activated mortars, Construction and Building Materials. 265 (2020) 120320. https://doi.org/10.1016/J.CONBUILDMAT.2020.120320.

[4] Z. Li, T. Lu, X. Liang, H. Dong, G. Ye, Mechanisms of autogenous shrinkage of alkali-activated slag and fly ash pastes, Cement and Concrete Research. 135 (2020) 106107. https://doi.org/https://doi.org/10.1016/j.cemconres.2020.106107.

[5] W. Tu, Y. Zhu, G. Fang, X. Wang, M. Zhang, Internal curing of alkali-activated fly ash-slag pastes using superabsorbent polymer, Cement and Concrete Research. 116 (2019) 179–190. https://doi.org/https://doi.org/10.1016/j.cemconres.2018.11.018.

[6] L. Lei, H.-K. Chan, Investigation into the molecular design and plasticizing effectiveness of HPEG-based polycarboxylate superplasticizers in alkali-activated slag, Cement and Concrete Research. 136 (2020) 106150. https://doi.org/https://doi.org/10.1016/j.cemconres.2020.106150.

[7] Z. Giergiczny, Fly ash and slag, Cement and Concrete Research. 124 (2019) 105826. https://doi.org/https://doi.org/10.1016/j.cemconres.2019.105826.

[8] Y. Alrefaei, Y.S. Wang, J.G. Dai, The effectiveness of different superplasticizers in ambient cured one-part alkali activated pastes, Cement and Concrete Composites. 97 (2019) 166–174. https://doi.org/10.1016/J.CEMCONCOMP.2018.12.027.

[9] Y. Alrefaei, J.-G. Dai, Effects of delayed addition of polycarboxylate ether on one-part alkali-activated fly ash/slag pastes: Adsorption, reaction kinetics, and rheology, Construction and Building Materials. 323 (2022) 126611. https://doi.org/10.1016/J.CONBUILDMAT.2022.126611.

[10] L.P. Qian, L.Y. Xu, Y. Alrefaei, T. Wang, T. Ishida, J.G. Dai, Artificial alkali-activated aggregates developed from wastes and by-products: A state-of-the-art review, Resources, Conservation and Recycling. 177 (2022) 105971. https://doi.org/10.1016/J.RESCONREC.2021.105971.

[11] B. Walkley, R. San Nicolas, M.-A. Sani, G.J. Rees, J. v Hanna, J.S.J. van Deventer, J.L. Provis, Phase evolution of C-(N)-A-S-H/N-A-S-H gel blends investigated via alkali-activation of synthetic calcium aluminosilicate precursors, Cement and Concrete Research. 89 (2016) 120–135. https://doi.org/https://doi.org/10.1016/j.cemconres.2016.08.010.

[12] S.A. Bernal, J.L. Provis, B. Walkley, R. San Nicolas, J.D. Gehman, D.G. Brice, A.R. Kilcullen, P. Duxson, J.S.J. van Deventer, Gel nanostructure in alkali-activated binders based on slag and fly

ash, and effects of accelerated carbonation, Cement and Concrete Research. 53 (2013) 127–144. https://doi.org/https://doi.org/10.1016/j.cemconres.2013.06.007.

[13] P. Perez-Cortes, J.I. Escalante-Garcia, Gel composition and molecular structure of alkali-activated metakaolin-limestone cements, Cement and Concrete Research. 137 (2020) 106211. https://doi.org/https://doi.org/10.1016/j.cemconres.2020.106211.

[14] S. Puligilla, P. Mondal, Co-existence of aluminosilicate and calcium silicate gel characterized through selective dissolution and FTIR spectral subtraction, Cement and Concrete Research. 70 (2015) 39–49.

[15] W. Chen, B. Li, J. Wang, N. Thom, Effects of alkali dosage and silicate modulus on autogenous shrinkage of alkali-activated slag cement paste, Cement and Concrete Research. 141 (2021) 106322. https://doi.org/https://doi.org/10.1016/j.cemconres.2020.106322.

[16] Z. Shi, C. Shi, S. Wan, Z. Zhang, Effects of alkali dosage and silicate modulus on alkali-silica reaction in alkali-activated slag mortars, Cement and Concrete Research. 111 (2018) 104–115. https://doi.org/https://doi.org/10.1016/j.cemconres.2018.06.005.

[17] M. Fawer, M. Concannon, W. Rieber, Life cycle inventories for the production of sodium silicates, The International Journal of Life Cycle Assessment. 4 (1999) 207. https://doi.org/10.1007/BF02979498.

[18] R. Bajpai, K. Choudhary, A. Srivastava, K.S. Sangwan, M. Singh, Environmental impact assessment of fly ash and silica fume based geopolymer concrete, Journal of Cleaner Production. 254 (2020) 120147. https://doi.org/https://doi.org/10.1016/j.jclepro.2020.120147.

[19] Y.S. Wang, Y. Alrefaei, J.G. Dai, Roles of hybrid activators in improving the early-age properties of one-part geopolymer pastes, Construction and Building Materials. 306 (2021) 124880. https://doi.org/10.1016/J.CONBUILDMAT.2021.124880.

[20] M.F. Alnahhal, T. Kim, A. Hajimohammadi, Waste-derived activators for alkali-activated materials: A review, Cement and Concrete Composites. 118 (2021) 103980. https://doi.org/https://doi.org/10.1016/j.cemconcomp.2021.103980.

[21] M.F. Alnahhal, A. Hamdan, A. Hajimohammadi, T. Kim, Effect of rice husk ash-derived activator on the structural build-up of alkali activated materials, Cement and Concrete Research. 150 (2021) 106590. https://doi.org/https://doi.org/10.1016/j.cemconres.2021.106590.

[22] R.H. Geraldo, L.F.R. Fernandes, G. Camarini, Mechanical properties of porcelain waste alkali-activated mortar, Open Ceramics. 8 (2021) 100184. https://doi.org/https://doi.org/10.1016/j.oceram.2021.100184.

[23] I. Bianco, B. Ap Dafydd Tomos, R. Vinai, Analysis of the environmental impacts of alkali-activated concrete produced with waste glass-derived silicate activator – A LCA study, Journal of Cleaner Production. 316 (2021) 128383. https://doi.org/https://doi.org/10.1016/j.jclepro.2021.128383.

[24] G. di Bella, I. Arrigo, P. Catalfamo, F. Corigliano, L. Mavilia, Advances in the extraction of silica from glass cullet, in: Recycling and Reuse of Waste Materials, Thomas Telford Publishing, 2003: pp. 137–142.

[25] F. Puertas, M. Torres-Carrasco, Use of glass waste as an activator in the preparation of alkali-activated slag. Mechanical strength and paste characterisation, Cement and Concrete Research. 57 (2014) 95–104. https://doi.org/https://doi.org/10.1016/j.cemconres.2013.12.005.

[26] M. Torres-Carrasco, F. Puertas, Waste glass in the geopolymer preparation. Mechanical and microstructural characterisation, Journal of Cleaner Production. 90 (2015) 397–408. https://doi.org/https://doi.org/10.1016/j.jclepro.2014.11.074.

[27] H. MORI, Extraction of Silicon Dioxide from Waste Colored Glasses by Alkali Fusion Using Sodium Hydroxide, Journal of the Ceramic Society of Japan. 111 (2003) 376–381. https://doi.org/10.2109/jcersj.111.376.

[28] M. Keawthun, S. Krachodnok, A. Chaisena, Conversion of waste glasses into sodium silicate solutions, International Journal of Chemical Sciences. 12 (2014) 83–91. https://www.scopus.com/inward/record.uri?eid=2-s2.0-84896387397&partnerID=40&md5=0781919075a282f402202d83f1a87d76.

[29] B. Hu, S. Zhao, S. Zhang, Removal of lead from cathode ray tube funnel glass by generating the sodium silicate, J Air Waste Manage Assoc. 65 (2015) 106–114. https://doi.org/10.1080/10962247.2014.976721.

[30] R. Vinai, M. Soutsos, Production of sodium silicate powder from waste glass cullet for alkali activation of alternative binders, Cement and Concrete Research. 116 (2019) 45–56. https://doi.org/https://doi.org/10.1016/j.cemconres.2018.11.008.

[31] A. Fernández-Jiménez, N. Cristelo, T. Miranda, Á. Palomo, Sustainable alkali activated materials: Precursor and activator derived from industrial wastes, Journal of Cleaner Production. 162 (2017) 1200–1209. https://doi.org/https://doi.org/10.1016/j.jclepro.2017.06.151.

[32] R. Vinai, M. Soutsos, Production of sodium silicate powder from waste glass cullet for alkali activation of alternative binders, Cement and Concrete Research. 116 (2019) 45–56.

[33] J.C.B. Moraes, A. Font, L. Soriano, J.L. Akasaki, M.M. Tashima, J. Monzó, M. v Borrachero, J. Payá, New use of sugar cane straw ash in alkali-activated materials: A silica source for the preparation of the alkaline activator, Construction and Building Materials. 171 (2018) 611–621. https://doi.org/https://doi.org/10.1016/j.conbuildmat.2018.03.230.

[34] A. Maldonado-Alameda, J. Giro-Paloma, A. Rodríguez-Romero, J. Serret, A. Menargues, A. Andrés, J.M. Chimenos, Environmental potential assessment of MSWI bottom ash-based alkali-activated binders, Journal of Hazardous Materials. 416 (2021) 125828. https://doi.org/https://doi.org/10.1016/j.jhazmat.2021.125828.

[35] M.R. Ahmad, J. Lao, J.-G. Dai, D. Xuan, C.S. Poon, Upcycling of air pollution control residue waste into cementitious product through geopolymerization technology, Resources, Conservation and Recycling. 181 (2022) 106231. https://doi.org/10.1016/J.RESCONREC.2022.106231.

[36] E.P. Department, Waste-to-Energy, (2022). https://www.tpark.hk/en/process/ (accessed January 7, 2022).

[37] A. Bogush, J.A. Stegemann, I. Wood, A. Roy, Element composition and mineralogical characterisation of air pollution control residue from UK energy-from-waste facilities, Waste Management. 36 (2015) 119–129. https://doi.org/https://doi.org/10.1016/j.wasman.2014.11.017.

[38] A.J. Chandler, T.T. Eighmy, O. Hjelmar, D.S. Kosson, S.E. Sawell, J. Vehlow, H.A. van der Sloot, J. Hartlén, Municipal solid waste incinerator residues, Elsevier, 1997.

[39] MONITORING OF SOLID WASTE IN HONG KONG, Waste Statistics for 2020, 2020. https://www.wastereduction.gov.hk/sites/default/files/msw2020.pdf.

[40] J.A. Stegemann, The potential role of energy-from-waste air pollution control residues in the industrial ecology of cement, Journal of Sustainable Cement-Based Materials. 3 (2014) 111–127.

[41] M.J. Quina, J.M. Bordado, R.M. Quinta-Ferreira, Recycling of air pollution control residues from municipal solid waste incineration into lightweight aggregates, Waste Management. 34 (2014) 430–438. https://doi.org/https://doi.org/10.1016/j.wasman.2013.10.029.

[42] A.A. Bogush, J.A. Stegemann, Q. Zhou, Z. Wang, B. Zhang, T. Zhang, W. Zhang, J. Wei, Co-processing of raw and washed air pollution control residues from energy-from-waste facilities in the cement kiln, Journal of Cleaner Production. 254 (2020) 119924. https://doi.org/https://doi.org/10.1016/j.jclepro.2019.119924.

[43] K. I., A.R. D., B.A. R., C.C. R., Geopolymers from DC Plasma–Treated Air Pollution Control Residues, Metakaolin, and Granulated Blast Furnace Slag, Journal of Materials in Civil Engineering. 23 (2011) 735–740. https://doi.org/10.1061/(ASCE)MT.1943-5533.0000170.

[44] I. Kourti, D.A. Rani, D. Deegan, A.R. Boccaccini, C.R. Cheeseman, Production of geopolymers using glass produced from DC plasma treatment of air pollution control (APC) residues, Journal of Hazardous Materials. 176 (2010) 704–709. https://doi.org/https://doi.org/10.1016/j.jhazmat.2009.11.089.

[45] R. Shirley, L. Black, Alkali activated solidification/stabilisation of air pollution control residues and co-fired pulverised fuel ash, Journal of Hazardous Materials. 194 (2011) 232–242. https://doi.org/https://doi.org/10.1016/j.jhazmat.2011.07.100.

[46] J. Fu, M.W. Bligh, I. Shikhov, A.M. Jones, C. Holt, L.M. Keyte, F. Moghaddam, C.H. Arns, S.J. Foster, T.D. Waite, A microstructural investigation of a Na2SO4 activated cement-slag blend, Cement and Concrete Research. 150 (2021) 106609. https://doi.org/https://doi.org/10.1016/j.cemconres.2021.106609.

[47] Z. Shi, C. Shi, S. Wan, Z. Zhang, Effects of alkali dosage and silicate modulus on alkali-silica reaction in alkali-activated slag mortars, Cement and Concrete Research. 111 (2018) 104–115. https://doi.org/https://doi.org/10.1016/j.cemconres.2018.06.005.

[48] A. Rafeet, R. Vinai, M. Soutsos, W. Sha, Effects of slag substitution on physical and mechanical properties of fly ash-based alkali activated binders (AABs), Cement and Concrete Research. 122 (2019) 118–135. https://doi.org/https://doi.org/10.1016/j.cemconres.2019.05.003.

[49] X. Gao, Q.L. Yu, H.J.H. Brouwers, Apply 29Si, 27Al MAS NMR and selective dissolution in identifying the reaction degree of alkali activated slag-fly ash composites, Ceramics International. 43 (2017) 12408–12419. https://doi.org/https://doi.org/10.1016/j.ceramint.2017.06.108.

[50] M.R. Ahmad, B. Chen, J. Yu, A comprehensive study of basalt fiber reinforced magnesium phosphate cement incorporating ultrafine fly ash, Composites Part B: Engineering. 168 (2019) 204–217. https://doi.org/10.1016/j.compositesb.2018.12.065.

[51] J. Mills, P. Mondal, N. Wagner, Structure-property relationships and state behavior of alkali-activated aluminosilicate gels, Cement and Concrete Research. 151 (2022) 106618. https://doi.org/https://doi.org/10.1016/j.cemconres.2021.106618.

[52] S. Zhang, E. Duque-Redondo, A. Kostiuchenko, J.S. Dolado, G. Ye, Molecular dynamics and experimental study on the adhesion mechanism of polyvinyl alcohol (PVA) fiber in alkali-activated slag/fly ash, Cement and Concrete Research. 145 (2021) 106452. https://doi.org/https://doi.org/10.1016/j.cemconres.2021.106452.

[53] P.G. Mathews, Design of Experiments with MINITAB, ASQ Quality Press Milwaukee, WI, USA:, 2005.

[54] Z.R. Lazic, Design of experiments in chemical engineering: a practical guide, John Wiley & Sons, 2006.

[55] M. ben Haha, K. de Weerdt, B. Lothenbach, Quantification of the degree of reaction of fly ash, Cement and Concrete Research. 40 (2010) 1620–1629. https://doi.org/10.1016/J.CEMCONRES.2010.07.004.

[56] M. Criado, A. Fernández-Jiménez, A. Palomo, Alkali activation of fly ash: Effect of the SiO2/Na2O ratio: Part I: FTIR study, Microporous and Mesoporous Materials. 106 (2007) 180–191. https://doi.org/10.1016/J.MICROMESO.2007.02.055.

[57] C. Lu, Q. Wang, Y. Liu, T. Xue, Q. Yu, S. Chen, Influence of new organic alkali activators on microstructure and strength of fly ash geopolymer, Ceramics International. (2022). https://doi.org/10.1016/J.CERAMINT.2022.01.109.

[58] I. García Lodeiro, D.E. Macphee, A. Palomo, A. Fernández-Jiménez, Effect of alkalis on fresh C–S–H gels. FTIR analysis, Cement and Concrete Research. 39 (2009) 147–153. https://doi.org/10.1016/J.CEMCONRES.2009.01.003.

[59] R. Cao, S. Zhang, N. Banthia, Y. Zhang, Z. Zhang, Interpreting the early-age reaction process of alkali-activated slag by using combined embedded ultrasonic measurement, thermal analysis, XRD, FTIR and SEM, Composites Part B: Engineering. 186 (2020) 107840. https://doi.org/10.1016/J.COMPOSITESB.2020.107840.

[60] H. el Didamony, H.H. Assal, T.M. el Sokkary, H.A.A. Gawwad, Kinetics and physico-chemical properties of alkali activated blast-furnace slag/basalt pastes, Https://Doi.Org/10.1016/j.Hbrcj.2012.10.002. 8 (2019) 170–176. https://doi.org/10.1016/J.HBRCJ.2012.10.002.

[61] Z. Zhang, H. Wang, J.L. Provis, F. Bullen, A. Reid, Y. Zhu, Quantitative kinetic and structural analysis of geopolymers. Part 1. The activation of metakaolin with sodium hydroxide, Thermochimica Acta. 539 (2012) 23–33. https://doi.org/10.1016/J.TCA.2012.03.021.

[62] N. Granizo, A. Palomo, A. Fernandez-Jiménez, Effect of temperature and alkaline concentration on metakaolin leaching kinetics, Ceramics International. 40 (2014) 8975–8985. https://doi.org/10.1016/J.CERAMINT.2014.02.071.

[63] P. Duxson, J.L. Provis, G.C. Lukey, F. Separovic, J.S.J. van Deventer, 29Si NMR Study of Structural Ordering in Aluminosilicate Geopolymer Gels, Langmuir. 21 (2005) 3028–3036. https://doi.org/10.1021/LA047336X.

[64] M.A. Longhi, B. Walkley, E.D. Rodríguez, A.P. Kirchheim, Z. Zhang, H. Wang, New selective dissolution process to quantify reaction extent and product stability in metakaolin-based geopolymers, Composites Part B: Engineering. 176 (2019) 107172. https://doi.org/https://doi.org/10.1016/j.compositesb.2019.107172.

[65] V. Kocaba, E. Gallucci, K.L. Scrivener, Methods for determination of degree of reaction of slag in blended cement pastes, Cement and Concrete Research. 42 (2012) 511–525. https://doi.org/10.1016/J.CEMCONRES.2011.11.010.

[66] I. García-Lodeiro, A. Fernández-Jiménez, M.T. Blanco, A. Palomo, FTIR study of the sol-gel synthesis of cementitious gels: C-S-H and N-A-S-H, Journal of Sol-Gel Science and Technology. 45 (2008) 63–72. https://doi.org/10.1007/S10971-007-1643-6/TABLES/7.

[67] X. Chen, J. Wang, G.R. Zhu, S. Ding, H.Y. Zhang, F.Y. Xia, Mechanical Properties and Mechanisms of Polyacrylamide-Modified Granulated Blast Furnace Slag–Based Geopolymer, Journal of Materials in Civil Engineering. 31 (2018) 04018347. https://doi.org/10.1061/(ASCE)MT.1943-5533.0002564.

[68] S. Puligilla, P. Mondal, Role of slag in microstructural development and hardening of fly ash-slag geopolymer, Cement and Concrete Research. 43 (2013) 70–80. https://doi.org/10.1016/J.CEMCONRES.2012.10.004.

[69] C.K. Yip, G.C. Lukey, J.L. Provis, J.S.J. van Deventer, Effect of calcium silicate sources on geopolymerisation, Cement and Concrete Research. 38 (2008) 554–564. https://doi.org/10.1016/J.CEMCONRES.2007.11.001.

[70] J.E. Oh, J. Moon, S.G. Oh, S.M. Clark, P.J.M. Monteiro, Microstructural and compositional change of NaOH-activated high calcium fly ash by incorporating Na-aluminate and co-existence of geopolymeric gel and C–S–H(I), Cement and Concrete Research. 42 (2012) 673–685. https://doi.org/10.1016/J.CEMCONRES.2012.02.002.

[71] T.A. Aiken, J. Kwasny, W. Sha, M.N. Soutsos, Effect of slag content and activator dosage on the resistance of fly ash geopolymer binders to sulfuric acid attack, Cement and Concrete Research. 111 (2018) 23–40. https://doi.org/10.1016/J.CEMCONRES.2018.06.011.

[72] F.Z. Abir, M. Mesnaoui, Y. Abouliatim, L. Nibou, T. Labbilta, Y. el Hafiane, A. Smith, Effect of the addition of iron oxide on the microstructure of ye'elimite, Cement and Concrete Research. 151 (2022) 106625. https://doi.org/https://doi.org/10.1016/j.cemconres.2021.106625.

[73] Y. Sargam, K. Wang, Quantifying dispersion of nanosilica in hardened cement matrix using a novel SEM-EDS and image analysis-based methodology, Cement and Concrete Research. 147 (2021) 106524. https://doi.org/https://doi.org/10.1016/j.cemconres.2021.106524.

[74] G. Fang, M. Zhang, Multiscale micromechanical analysis of alkali-activated fly ash-slag paste, Cement and Concrete Research. 135 (2020) 106141. https://doi.org/https://doi.org/10.1016/j.cemconres.2020.106141.

[75] F. Puertas, M. Palacios, H. Manzano, J.S. Dolado, A. Rico, J. Rodríguez, A model for the C-A-S-H gel formed in alkali-activated slag cements, J Eur Ceram Soc. 31 (2011) 2043–2056. https://doi.org/https://doi.org/10.1016/j.jeurceramsoc.2011.04.036.

[76] Z. Zhang, L. Li, X. Ma, H. Wang, Compositional, microstructural and mechanical properties of ambient condition cured alkali-activated cement, Construction and Building Materials. 113 (2016) 237–245.

[77] M. Nedeljković, B. Šavija, Y. Zuo, M. Luković, G. Ye, Effect of natural carbonation on the pore structure and elastic modulus of the alkali-activated fly ash and slag pastes, Construction and Building Materials. 161 (2018) 687–704. https://doi.org/https://doi.org/10.1016/j.conbuildmat.2017.12.005.

[78] G.A. Lyngdoh, S. Nayak, N.M.A. Krishnan, S. Das, Fracture toughness of fly ash-based geopolymer gels: Evaluations using nanoindentation experiment and molecular dynamics simulation, Construction and Building Materials. 262 (2020) 120797. https://doi.org/https://doi.org/10.1016/j.conbuildmat.2020.120797.

[79] G. Fang, Q. Wang, M. Zhang, Micromechanical analysis of interfacial transition zone in alkali-activated fly ash-slag concrete, Cement and Concrete Composites. 119 (2021) 103990. https://doi.org/https://doi.org/10.1016/j.cemconcomp.2021.103990.

[80] J. Němeček, V. Šmilauer, L. Kopecký, Nanoindentation characteristics of alkali-activated aluminosilicate materials, Cement and Concrete Composites. 33 (2011) 163–170. https://doi.org/https://doi.org/10.1016/j.cemconcomp.2010.10.005.

[81] I. Hager, M. Sitarz, K. Mróz, Fly-ash based geopolymer mortar for high-temperature application – Effect of slag addition, Journal of Cleaner Production. 316 (2021) 128168. https://doi.org/https://doi.org/10.1016/j.jclepro.2021.128168.

[82] J.C. Kuri, S. Majhi, P.K. Sarker, A. Mukherjee, Microstructural and non-destructive investigation of the effect of high temperature exposure on ground ferronickel slag blended fly ash geopolymer mortars, Journal of Building Engineering. 43 (2021) 103099. https://doi.org/https://doi.org/10.1016/j.jobe.2021.103099.